Title

PARP1-mediated PARylation activity is essential for oligodendroglial differentiation and CNS myelination

Permalink

https://escholarship.org/uc/item/00q9t3t8

Journal

Cell Reports, 37(1)

ISSN

2639-1856

Authors

Wang, Yan
Zhang, Yanhong
Zhang, Sheng
et al.

Publication Date

2021-10-01

DOI

10.1016/j.celrep.2021.109695

Peer reviewed

PARP1-mediated PARylation activity is essential for oligodendroglial differentiation and CNS myelination

Yan Wang[1,4], **Yanhong Zhang**[1,4], **Sheng Zhang**[1,4], **Bokyung Kim**[1,4], **Vanessa L. Hull**[1,4], **Jie Xu**[4], **Preeti Prabhu**[1,4], **Maria Gregory**[1,4], **Veronica Martinez-Cerdeno**[2,4], **Xinhua Zhan**[1], **Wenbin Deng**[3,5], **Fuzheng Guo**[1,4,6,*]

[1]Department of Neurology, School of Medicine, University of California, Davis, Davis, CA 95817, USA

[2]Department of Pathology and Laboratory Medicine, University of California, Davis, Davis, CA 95817, USA

[3]Biochemistry and Molecular Medicine, School of Medicine, University of California, Davis, CA 95817, USA

[4]Institute for Pediatric Regenerative Medicine (IPRM), Shriners Hospitals for Children, Sacramento, CA 95817, USA

[5]Present address: School of Pharmaceutical Sciences (Shenzhen), Sun Yat-sen University, Guangzhou 510275, China

[6]Lead contact

SUMMARY

The function of poly(ADP-ribosyl) polymerase 1 (PARP1) in myelination and remyelination of the central nervous system (CNS) remains enigmatic. Here, we report that PARP1 is an intrinsic driver for oligodendroglial development and myelination. Genetic PARP1 depletion impairs the differentiation of oligodendrocyte progenitor cells (OPCs) into oligodendrocytes and impedes CNS myelination. Mechanistically, PARP1-mediated PARylation activity is not only necessary but also sufficient for OPC differentiation. At the molecular level, we identify the RNA-binding protein Myef2 as a PARylated target, which controls OPC differentiation through the PARylation-modulated derepression of myelin protein expression. Furthermore, PARP1's enzymatic activity is necessary for oligodendrocyte and myelin regeneration after demyelination. Together, our findings suggest that PARP1-mediated PARylation activity may be a potential therapeutic target

for promoting OPC differentiation and remyelination in neurological disorders characterized by arrested OPC differentiation and remyelination failure such as multiple sclerosis.

In brief

Wang et al. show that PARP1-mediated PARylation promotes oligodendroglial differentiation and regeneration. They demonstrate that PARP1 PARylates proteins relating to RNA metabolism under physiological conditions and that Myef2 is identified as one of the potential targets that mediates PARP1-regulated myelin gene expression at the posttranscriptional level during oligodendroglial development.

Graphical Abstract
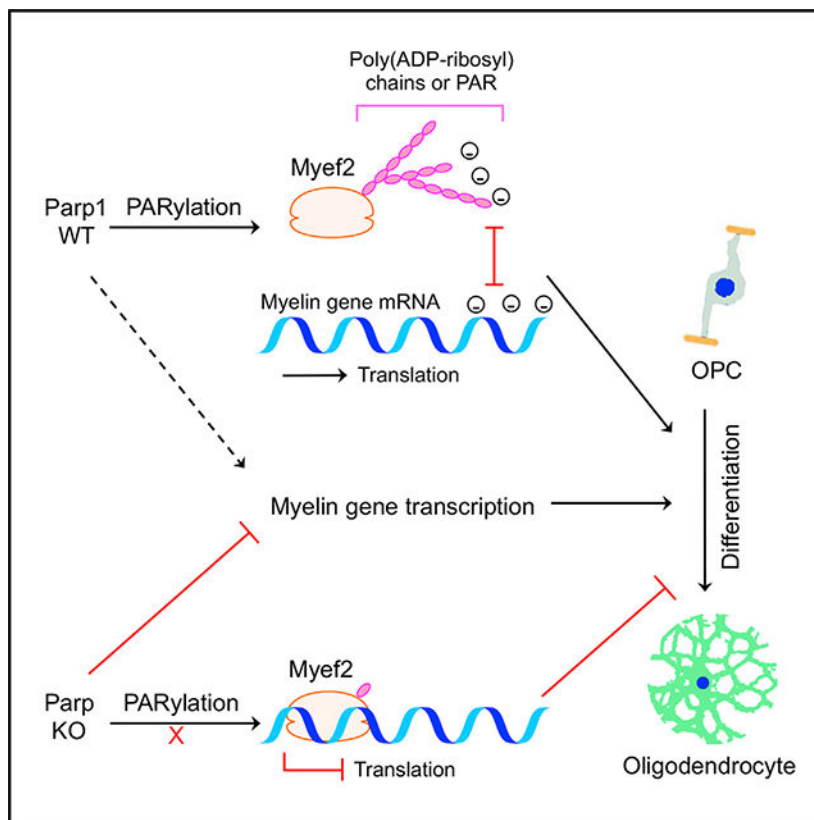
INTRODUCTION

Poly(ADP-ribosyl) polymerase 1 (PARP1) is the founding member of the PARP family, which consists of 17 members that transfer mono(ADP-ribose) or poly(ADP-ribose) (PAR) units to target proteins (Gupte et al., 2017). PARP1 is one of only four members (PARP1, PARP2, PARP5a, and PARP5b) that catalyze the covalent attachment of PAR onto target proteins, a process called PARylation (Ke et al., 2019). PARP1 has been reported to be responsible for >90% of cellular PARylation in non-neural tissues (Kamaletdinova et al., 2019), which can be reversed by the activity of the degrading enzyme PAR glycohydrolase (PARG) (Davidovic et al., 2001). Initially discovered as an essential player for DNA repair

in cancer cells, PARP1 has been increasingly recognized as a key regulator for diverse cellular processes such as chromatin remodeling, gene expression regulation, and cell death/survival (Gupte et al., 2017). Despite the growing knowledge of its basic molecular functions, the physiological role and significance of PARP1 in oligodendroglial development and myelinogenesis are poorly defined.

In the murine central nervous system (CNS), developmental myelination starts from the 2nd postnatal week, peaks around one month, and completes in the early adult ages (Salmaso et al., 2014; Semple et al., 2013). In the developing murine CNS, PARP1 is expressed in all types of neural cells, with the highest abundance in oligodendroglial lineage cells (OLCs) (Zhang et al., 2014). Under demyelinating conditions, PARP1 and/or its PARylation activity has been reported to be upregulated in various neural and immune cells in the inflammatory demyelinating disease multiple sclerosis (MS) (Farez et al., 2009; Meira et al., 2019; Veto et al., 2010). In the past 3 decades, the role of PARP1 in regulating neuroinflammation has been extensively studied (Cavone and Chiarugi, 2012). However, little is known about if and how PARP1 regulates oligodendroglial development and CNS myelinogenesis. We previously showed that PARP1 deficiency increased oligodendrocyte (OL) progenitor cell (OPC) generation from neural stem cells (NSCs) yet decreased myelin basic protein (MBP) expression in the brain of global *Parp1* knockout (KO) mice (Plane et al., 2012). Recent data reported that inhibiting PARP1 impaired OL maturation in mixed glial cell cultures derived from NSCs (Baldassarro et al., 2017). These data suggest that PARP1 may play a role in oligodendroglial lineage development.

Here, we showed that, in contrast to its role in cell death/survival under genotoxic conditions, PARP1 is an intrinsic driver for OL development. PARP1's PARylation activity plays a key role in PARP1-regulated differentiation of OPC into OLs in a cell-autonomous manner. Molecularly, we unveiled that PARP1 PARylates Myef2 and dissociates it from myelin gene mRNAs, relieving its suppressive effects on myelin protein expression. Our findings suggest that augmenting PARP1 and/or its activity-mediated PARylation might be a viable option to enhance OPC differentiation and remyelination in demyelinating disorders.

RESULTS

PARP1 is dynamically expressed in OL lineage

Through an effort to screen the interactome of Sox2 (Figure S1A), which we previously reported to promote oligodendrogenesis (Zhang et al., 2018a, 2018b), we identified PARP1 as one of the top candidates (Figure S1; Table S1). The expression dynamics of PARP1 in OLCs has yet to be defined. PARP1 was highly expressed during developmental myelination and progressively downregulated after myelination completion (Figure 1A). Within OLCs, PARP1 expression was low in PDGFRα[+] OPCs (Figure 1B, arrowheads); elevated in CC1^{+} premyelinating OLs (Figure 1B, arrows), which was confirmed by a premyelinating OL marker TCF7l2 (Hammond et al., 2015) (Figure 1C, arrowheads); and downregulated in fully mature myelinating OLs in the adult spinal cord where PARP1 was maintained at a low-level in PDGFRα[+] OPCs (Figure 1D). The dynamic expression along OL lineage progression and maturation (Figure 1G) was confirmed by primary OPC cultures (Figures 1E and 1F) purified from neonatal mouse brain (Lang et al., 2013; Zhang et al., 2021b).

PARP1 deficiency results in impaired OL maturation and hypomyelination

To elucidate the importance of PARP1 in developmental myelination, we characterized oligodendrogenesis and myelin formation in *Parp1* KO mice (Plane et al., 2012; Wang et al., 1995), which were confirmed by the absence of PARP1 protein (Figure 2A) and mRNA (Figure 2B). We observed prominent hypomyelination in the brain of postnatal day 10 (P10) *Parp1* KO mice compared with wild-type (WT) littermates (Figure 2C). The density of Sox10$^+$CC1$^+$ differentiated OLs but not Sox10$^+$PDGFRα$^+$ OPCs was significantly diminished in the corpus callosum (CC) of P10 *Parp1* KO mice (Figure 2D), suggesting that PARP1 regulates oligodendroglial maturation. Consistently, we found a marked decrease in the brain mRNA levels of major myelin proteins (Figure 2E). The nuclear protein TCF7l2 is selectively expressed in newly formed OLs (Hammond et al., 2015; Marques et al., 2016; Zhao et al., 2016). Hence, the number of TCF7l2$^+$ OLs at any given time provides a quantitative readout for the oligodendrogenesis rate. We observed a significant diminution of TCF7l2$^+$Sox10$^+$ cell density in the CC of P10 *Parp1* KO mice (Figure 2F). Furthermore, the expression of other marker genes enriched in newly formed OLs was also reduced in the P10 *Parp1* KO brain (Figure 2G). These data suggest that PARP1 deficiency inhibits OL maturation and developmental myelination.

Next, we performed a time-course analysis at the time windows of developmental myelination peak (at P30) and myelination completion (at P70). Brain myelination, assessed by Black-Gold II myelin staining, was reduced in the CC of *Parp1* KO mice at P30 (Figure 2H), which was confirmed by toluidine blue myelin staining (Zhang et al., 2021a) (Figure S2A). Consistent with the hypomyelination phenotype, the number of Sox10$^+$CC1$^+$-differentiated OLs was diminished in the CC (Figure 2I). CNS hypomyelination is associated with motor dysfunction of developing mice (Fancy et al., 2009; Moyon et al., 2016; Wang et al., 2018; Zhang et al., 2018b), which can be quantified by the sensitive rotarod test (Kuhn et al., 1995). The rotarod test showed that P30 *Parp1* KO mice displayed a defective motor performance (Figures S2B and S2C). At P70, a time point at which developmental myelination is already completed in the murine CNS, we observed a similar OL population (Figure S2D) and myelin gene expression (Figure S2E) in *Parp1* KO mice to those in WT mice. Myelination in the adult brain, assessed by Black-Gold II myelin staining (Figure S2F), was comparable between the 2 groups, which was confirmed by transmission electron microscopy (TEM) (Figure S2G1–S2G3). However, the myelin sheath is thinner, as evidenced by a greater g-ratio (Figure S2G4), in *Parp1* KO than in that of WT mice. Motor function, evaluated by rotarod test, was still impaired in adult *Parp1* KO mice (Figure S2H and S2I). Together, the time-course analysis suggests that PARP1 deficiency delays OPC differentiation and developmental myelination.

PARP1 is a cell intrinsic regulator for OL maturation

To determine if PARP1 regulates OL maturation in a cell autonomous manner, we sought to use primary OPC cultures purified from neonatal *Parp1* KO and WT brain (Figure 2J). PARP1 depletion did not affect the expression of the family members PARP2 or PARP3 (Figure 2K). Strikingly, when cultured in the differentiation medium (DM) for 3 days, PARP1-depleted OPCs exhibited severe inhibition of differentiation and maturation, as evidenced by a reduced percentage of MBP$^+$ OLs with arborized morphology (Figure

2L) and diminished expression of major myelin proteins (Figure 2M). No difference in the expression of astrocyte-specific genes *Aldh1l1, Gfap*, and *Aqp4* (Figure 2N) was observed, suggesting that PARP1-depleted OPCs do not switch their fate to astroglial lineage. Collectively, our data indicate that PARP1 regulates oligodendroglial differentiation and maturation in a cell-autonomous fashion.

PARP1 cKO in Olig2-expressing cells inhibits oligodendrogenesis

We next employed *Cre-loxP*-based conditional KO (cKO) to elucidate PARP1's role in oligodendroglial development. To this end, we crossed *Olig2-Cre* (Schüller et al., 2008) with *Parp1*-floxed (Luo et al., 2017) mice to deplete PARP1 selectively in Olig2-expressing primitive OPCs starting from the embryonic stages (Rowitch, 2004). A fate-mapping study showed that *Olig2-Cre*-mediated recombination was observed in ~80% of Sox10$^+$ OLCs in the CC of *Olig2-Cre:Rosa26-EYFP* mice at P17 (Figures S3A and S3B), which is in line with previous data (Chavali et al., 2020; Fancy et al., 2014). *Olig2-Cre:Parp1* cKO (Figure S3C) resulted in hypomyelination (Figure S3D) and defective oligodendroglial maturation (Figure S3E) in the brain at P14, a time point corresponding to the developmental myelination onset in mice. A time-course analysis demonstrated that oligodendroglial differentiation and developmental myelination were inhibited in the CNS of *Olig2-Cre:Parp1* cKO mice at P30 (Figures S3F and S3G) and returned to the WT level at P70 (Figures S3H and S3I). A TEM assay confirmed that the number of myelinated axons and total axons was similar in the corticospinal tract (CST) (Figure S3J1–S3J3) and CC (Figures S3K1–S3K3) between the two groups at P70. However, the myelin sheath was thinner, as evidenced by a greater g-ratio, in both areas of *Parp1* cKO mice than in that of control (Ctrl) mice (Figures S3J4 and S3K4). Both developing and adult *Olig2-Cre:Parp1* cKO mice developed defective motor performance (Figures S3L and S3M), but they displayed normal ability of motor skill earning (Figure S3M). Collectively, our data suggest that PARP1 expression in Olig2-expressing cells is required for developmental myelination in early postnatal mice and motor function in adult mice, as well.

PARP1 regulates OPC differentiation into OLs in the postnatal CNS

OLs are differentiated from OPCs that are generated from cortical progenitors in the murine brain during early postnatal development (Kessaris et al., 2006). To determine the role of PARP1 in postnatal OPC differentiation, we generated *Pdgfra-CreER^{T2}:Parp1$^{fl/fl}$* (*Pdgfra:Parp1* cKO) mutants, thus enabling the time-conditional depletion of PARP1 in OPCs by tamoxifen treatment (Figures 3A and 3B). Tamoxifen administration at P1, P2, and P3 resulted in PARP1 depletion in 89.6% ± 7.4% (n = 4 mice) PDGFRα$^+$ OPCs in the CC (Figure 3C). Gene Ontology (GO) analysis of bulk-brain RNA sequencing (RNA-seq) data (Table S2) showed that OPC differentiation and myelination were overrepresented among the downregulated genes in the *Pdgfra:Parp1* cKO brain (Figure 3D). The expression of major myelin-specific genes (Figure 3E) and premyelinating OL-enriched genes (Figure 3F) was severely affected in the *Pdgfra: Parp1* cKO brain. Moreover, the number of Sox10$^+$CC1$^+$-differentiated OLs (Figure 3G) and TCF7l2$^+$ newly generated OLs (Figure 3H) was decreased in the CC of *Pdgfra:Parp1* cKO mice. Consistently, MBP was observed at a reduced level in the subcortical white matter of the *Pdgfra:Parp1* cKO brain whereas SMI312$^+$ axonal bundles were comparable (Figure 3I). OPC-specific PARP1 depletion did

not affect oligodendroglial proliferation (Figures S4A and S4B), cell death (Figures S4C and S4D), or microglial (Figures S4E–S4G) and astroglial (Figures S4H–S4J) activation. We also found a significant reduction in the density of Sox10^{+}CC1^{+} OLs (Figure 3J) and the expression of myelin-associated genes (Figure 3K) and newly formed OL marker genes (Figure 3L) in the spinal cord of *Pdgfra:PARP1* cKO mice. Altogether, these data demonstrate that PARP1 is required for OPC differentiation not only in the brain but also in the spinal cord.

Oligodendroglial PARP1 is essential for developmental myelination

Developmental myelination in the murine CNS starts approximately at the beginning of the 2nd week after birth. Therefore, we analyzed oligodendroglial myelin formation at P14 in the CST of *Pdgfra:Parp1* cKO mice that received tamoxifen at P6/P7 (Figure 3M). Toluidine blue myelin staining demonstrated a significant decrease of the myelinated axon number in *Pdgfra:Parp1* cKO mice (Figure 3N), which was confirmed by TEM assay (Figure 3O). The density of total axons with a diameter ≥ 0.3 μm was comparable between *Pdgfra:Parp1* cKO mice and Ctrls (Figure 3P). Among the myelinated axons, the myelin sheath was significantly thinner, as evidenced by a greater g-ratio in *Pdgfra:Parp1* cKO mice than in that of *Parp1* Ctrls (Figures 3Q and 3R). These data collectively suggest that PARP1 is required for oligodendroglial myelination.

PARP1 is activated primarily in OLCs during postnatal CNS development

To elucidate the mechanisms underlying PARP1-regulated oligodendroglial development, we sought to interrogate if PARP1's activity plays a part. We employed PAR immunedetection as a reliable surrogate for PARP1's enzymatic activation (Figure 4A) (Luo and Kraus, 2012). The absence of PAR^{+} cells in the spinal cord of *Parp1* KO mice (Figure 4B) revealed that PARP1 is the major PARP family member responsible for cellular PARylation activity in the CNS. We next used lineage-specific markers to determine what cell type exhibits PARP1 activity. The vast majority of PAR^{+} cells (94.5% ± 5.2%, n = 3) were Sox10-expressing OLCs in the developing spinal white matter. The PAR signal was low in PDGFRα[+] OPCs, elevated in CC1^{+} OLs (Figure 4C) in the spinal cord at P7 (relative PAR intensity in OPCs 1.0 ± 0.08 versus OLs 4.1 ± 0.25, $p < 0.0001$, n = 36 cells), and became undetectable in the adult spinal cord (Figure 4D). The dynamic pattern of PAR was confirmed by primary OL cultures purified from neonatal rodent brain: low in OPCs, elevated in newly formed immature OLs (D1 and D2), and downregulated in mature OLs (D4) (Figure 4E). Our data are in line with a previous report that PARP1 activity is higher in neonatal OPCs than in adult OPCs (Baldassarro et al., 2017). Thus, PARP1 is transiently activated primarily in OLCs during postnatal CNS development.

PARP1 hyperactivation in response to excessive DNA damaging agents leads to cell death in a context-dependent manner (Alano et al., 2010; Hassa, 2009; Scott et al., 2003). We found that the morphology of PAR[+]Sox10^{+} nuclei (Figure 4F, arrowheads) was indistinguishable from that of PAR[−]Sox10^{+} nuclei (Figure 4F, arrows), both of which exhibited no morphological characteristics of dying cells, such as nuclear condensation (Figure 4G, arrowheads), suggesting that PARP1 activation may be dispensable for OL death in the developing CNS where minimal genotoxic injury exists.

PARP1 enzymatic activity is required for OPC differentiation

To elucidate the function of PARP1 activity in oligodendroglial development, we used the potent PARP1 inhibitor 4-hydroxyquinazoline (4HQ) to dampen cellular PARylation (Figure 4A) and determined the cell-autonomous effect on OPC differentiation in purified primary OPC cultures (Figure 4H). 4HQ treatment remarkably reduced the PAR signal (Figure 4I) without affecting PARP1 expression (Figure 4J). The percent of ramified MBP$^+$ OLs was decreased (Figure 4I), and myelin-specific gene expression was diminished (Figure 4J) in the 4HQ-treated group. An MTT cell viability assay demonstrated that the 4HQ concentration we used (10 μM) had no effect on OL death (Figure 4K). These *in vitro* data suggest that the PARP1 activity-dependent function plays a crucial role in PARP1-regulated OPC differentiation.

We next determined whether PARP1 activity regulates OPC differentiation *in vivo*. A 4HQ injection into neonatal mice (Figure 4L) significantly decreased the number of Sox10$^+$ OLCs that were positive for PAR (Figure 4O) without perturbing PARP1 expression (Figures 4M and 4N). Myelination, visualized by MBP staining, was significantly reduced in the subcortical white matter of 4HQ-treated mice (Figure 4P). We found a significant reduction in the density of CC1$^+$-differentiated OLs (Figure 4Q), the expression of myelin-specific genes (Figure 4R), and the density of TCF7l2$^+$-premyelinating OLs (Figure 4S) in the brain of 4HQ-treated mice. Moreover, the number of OLs was significantly diminished in the spinal cord of 4HQ-treated mice compared with that in the Ctrl spinal cord (Figure 4T). Our further analysis showed that PARP1 inhibition did not affect cell death and glial activation (Figure S5). Collectively, these data suggest that PARP1 enzymatic activity is essential for OPC differentiation and that PARP1 activation plays a minor role in mediating cell death and glial activation during CNS developmental myelination.

PARylation stabilization promotes OPC differentiation

The half-life of PAR chains deposited on acceptor proteins by PARP1 is less than 1 minute (Zhen and Yu, 2018). The rapid turnover is catalyzed by PARG (Figure 5A). We next asked if stabilizing PARylation affects OPC differentiation. To this end, we used a potent PARG inhibitor, PDD 00017273 (PDD) (James et al., 2016) (Figure 5B) to augment PARylation through dampening PAR degradation (Figure 5C). PDD treatment increased the number (Ctrl, 405 ± 33 [n = 5] versus PDD, 572 ± 43 [n = 6], p = 0.016) and intensity of the PAR signal in Sox10$^+$ OLCs (Figure 5D). Strikingly, we found that the density of CC1$^+$ OLs was significantly increased in the ventral white matter of spinal cord and the forebrain CC of PDD-treated mice (Figure 5E), whereas PDGFRα$^+$ OPCs were not affected (Figure 5F). The density of myelinated axons (Figure 5G, arrowheads) was significantly increased in the CST of PDD-treated mice (Figure 5G, right panel), as assessed by high-power confocal images of MBP (myelin) and SMI312 (axons). Together, these data indicate that augmenting cellular PARylation level promotes oligodendrogenesis and accelerates developmental myelination.

To determine whether stabilizing PARylation affects OPC differentiation in a cell-autonomous fashion, we sought to use purified primary OPC cultures (Figure 5H) treated with a non-toxic concentration of PDD (1 μM) (Figure 5I). PDD treatment markedly increased the PAR signal (Figure 5J) without altering PARP1 and PARG expression (Figure

5K). We found that PDD inhibition promoted OPC differentiation and maturation, as evidenced by a significant increase in the percentage of MBP-expressing OLs bearing arborized morphology (Figure 5L), the mRNA levels of major myelin proteins (Figure 5M), and the protein levels of PLP, MAG, and TCF7l2 (Figure 5N). To strengthen the conclusion, siRNA-mediated PARG knockdown in purified primary rodent OPCs (Figure 5O) significantly increased the expression of major myelin genes (*Mbp, Cnp*, and *Mag*) and the potent pro-differentiation factor *Myrf* (Figure 5P). Taken together, stabilizing PARP1-mediated PARylation promotes OPC differentiation.

Unbiased proteomics identifies target proteins of PARP1 activity

PARP1 activity regulates cellular processes mainly through binding to and modulating its PARylated target proteins (Luo and Kraus, 2012). We next sought to identify potential PAR acceptor (target) proteins, providing further molecular mechanisms underlying PARP1-regulated oligodendroglial development. To this end, PAR antibody Co-immunoprecipitation (co-IP) was used to enrich PARylated proteins from the P7 spinal cord where PAR$^+$ cells were identified as OLs (Figure 4C), followed by protein identification by liquid chromatography-tandem mass spectrometry (LC-MS/MS) (Figure 6A). We identified 131 potential PARylated nuclear proteins that were significantly enriched by at least 3-fold ($p < 0.05$) in PAR antibody IP components compared with immunoglobulin G (IgG) IP components (Table S3). GO analysis showed that the identified PAR acceptor proteins were predominantly associated with mRNA processing, splicing, transporting, and translation (Figure 6B) and participated in RNA binding function (Figure 6C). This is in stark contrast to the PARylated proteins previously identified from cells treated by the genotoxic agent H_2O_2 (Zhang et al., 2013), which were primarily related to DNA damage and repair (Figure S6).

Among the candidates (Table S3) were well-known acceptor proteins including PARP1, the prime PAR acceptor protein in cells (Luo and Kraus, 2012), histone proteins (histone H1.3 and H1fx), and heterogeneous nuclear ribonucleoproteins (hnRNPs) (Ke et al., 2019) (Figure 6D), which provides positive Ctrls for our unbiased approaches. Interestingly, we identified some PARylated proteins with reported functions in oligodendroglial development, such as Fus (Guzman et al., 2020), Mecp2 (Nguyen et al., 2013), Qki (Thangaraj et al., 2017; Zhou et al., 2020), and Fmr1 (Giampetruzzi et al., 2013; Shi et al., 2019) (Figure 6D). We also identified PARP1 target proteins with yet unknown functions in oligodendroglial development, such as the myelin expression factor 2 (Myef2), Y-box binding proteins (Ybx3 and Ybx2), polyadenylate-binding protein 1 (Pabpc1) (Figure 6D), and others (Table S3). Together, our data suggest a potential role of PARP1 in regulating RNA metabolism and RNA binding under physiological conditions and provide further PARP1 target proteins for future studies.

Myef2 is a PARP1 target, negatively regulating oligodendroglial differentiation

We next focused on Myef2 for further study. Co-IP/western blot (WB) assays confirmed that Myef2 interacted with PARP1 and was PARylated by PARP1 in primary OLs (Figure 6E). Using rodent primary cultures, we showed that Myef2 expression was downregulated along oligodendroglial lineage progression and maturation (Figure 6F). We found that genetic

Parp1 KO did not affect Myef2 expression (Figure 6G). These data suggest that, instead of regulating Myef2 expression, PARP1 may modulate its function through adding negatively charged PAR chains.

Recent data suggest that Myef2 binds to the majority mRNAs of protein-coding genes in oligodendroglial cell lines through 3′ untranslated region (UTR) (Samudyata et al., 2019), which often involves repressing mRNA processing and translation (Abaza and Gebauer, 2008; Szostak and Gebauer, 2013). We hypothesize that Myef2 may bind to myelin gene mRNAs and regulate myelin gene expression posttranscriptionally. We employed RNA IP (He et al., 2017) to pull down the Myef2-bound mRNA from D2 primary OLs and found that the myelin gene mRNA transcripts of *Mbp* and *Mag* were markedly enriched in Myef2 antibody components (Figure 6H). Notably, inhibiting PARP1's PARylation activity by 4HQ significantly enhanced the binding of Myef2 to *Mbp* and *Mag* mRNAs (Figure 6H), indicating that PARP1-mediated Myef2 PARylation dissociates Myef2 from binding myelin gene transcripts (Figure 6I).

To determine the role of Myef2 in oligodendroglial development, we employed siRNA-mediated knockdown in rodent primary OPC cultures (Figures 6J and 6K). We found that the percentage of MBP$^+$ cells (Figure 6L) was markedly increased in *Myef2* siRNA cultures (Figure 6M), which is corroborated by a significant increase of the myelin gene proteins MBP and MAG (Figures 6N and 6O). In contrast, the mRNA levels of *Mbp* and *Mag* were not affected by *Myef2* knockdown (Figure 6P), suggesting that Myef2 negatively regulates OPC differentiation by repressing myelin gene expression at the posttranscriptional level. Furthermore, our rescue experiment demonstrated that *Myef2* knockdown significantly relieved the degree of myelin protein (MBP and MAG) inhibition elicited by 4HQ (Figures 6Q and 6R). Altogether, our data indicate that PARP1's PARylation activity positively regulates OL maturation, at least in part, through PARylating Myef2 and subsequently relieving the repressive effect of Myef2 on myelin protein expression (Figure 6I).

Temporal dynamics of PARP1 activity during myelin damage and repair

To determine the significance of PARP1 activity in OL regeneration and remyelination, we employed the mouse model of cuprizone (CPZ)-induced demyelination. We first performed a time-course analysis of PARP1 activity during CPZ-induced demyelination and subsequent remyelination (Figure 7A). PARP1 activity, assessed by PAR immunohistochemistry (IHC), was absent from the CC of healthy adult mice (Figure 7B), markedly elevated during demyelination (Figures 7C and 7D) and active remyelination (Figure 7E), and progressively downregulated to a barely detectable level after remyelination was completed (Figure 7F). PAR signals were primarily observed in CD68$^+$ activated microglia (Figure 7D) and absent from Sox10$^+$ OLCs (Figure 7C) after 3 weeks of CPZ-induced demyelination. In contrast, PAR signals were induced primarily in Sox10-expressing OLCs (91.6% ± 7.9% of PAR$^+$ cells are Sox10$^+$, n = 4) at 1 week after returning to the normal diet (6+1 weeks), a time point at which active OL regeneration and remyelination occur in the CC. Triple IHC demonstrated that PAR signals were higher in CC1$^+$ newly regenerated OLs (Figure 7E, arrowheads) than PDGFRα$^+$ OPCs at 6+1 weeks (relative PAR intensity: OPCs 1.00 ± 0.09 versus OL 6.01 ± 0.36, p < 0.0001). The temporal dynamics of PARP1 activity within OLCs

is reminiscent of that during developmental myelination (Figure 4) and suggests that PARP1 activity may regulate OL regeneration and myelin repair.

PARP1 is required for OL regeneration and remyelination

To interrogate the role of PARP1 in remyelination, we treated CPZ-demyelinated mice with 4HQ on day 1 after returning to the normal diet for 7 days. The treated mice were analyzed 2 hours after the last 4HQ daily injection (Figure 7G). 4HQ treatment reduced PARP1's PARylation activity, as evidenced by a significant diminution of the PAR signal (Figure 7H). 4HQ inhibition impaired myelin repair assessed by Black-Gold II myelin assay (Figure 7I) and decreased the number of Sox10$^+$CC1$^+$ total OLs (Figure 7K) and TCF7l2$^+$ newly regenerated premyelinating OLs (Figure 7L) in the CC of CPZ+4HQ group compared with the CPZ+Veh group, whereas the number of PDGFRα$^+$Sox10$^+$ OPCs was comparable (Figure 7J). We found that the 4HQ-treatment paradigm we used did not affect the activation of microglia/macrophages quantified by Iba1 compared with that in the CPZ+Veh group (Figure S7A). These data indicate that PARP1 activity is required for OL regeneration and remyelination.

We next employed genetic PARP1 deletion to corroborate our conclusion derived from pharmacological inhibition. Tamoxifen-induced OPC-specific PARP1 deletion significantly reduced myelin repair, as assessed by Black-Gold II myelin staining (Figure 7M), and decreased the number of Sox10$^+$CC1$^+$ OLs in the CC of *Pdgfra:Parp1* cKO mice (Figure S7C), while the number of Sox10$^+$PDGFRα$^+$ OPCs was comparable to that of Ctrl mice (Figure S7D). Together, 4HQ inhibition and PARP1 deletion data suggest that PARP1-mediated PARylation is required for OL regeneration and myelin repair in the CPZ model.

DISCUSSION

The physiological and pathophysiological role of PARP1 in oligodendroglial development remains enigmatic. Using genetic and pharmacological approaches, we identify PARP1 as an intrinsic driver for OL differentiation and myelination. PARP1's PARylation activity plays an essential role in PARP1-regulated oligodendroglial development. We found that PARP1 PARylates its downstream target proteins that are involved in RNA metabolism and identified Myef2 as a PARylated target, which controls OPC differentiation by PARylation-modulated myelin gene expression. Thus, our studies unravel previously unappreciated functions of PARP1 in oligodendroglial development and CNS myelination and suggest that the PARP1-mediated pathway may be a potential therapeutic target for myelin repair in demyelinating disorders.

PARP1 activity is tightly controlled in OLCs and plays a minor role in OL death

PARP1 is activated primarily in OLCs during developmental myelination and remyelination. PARP1-mediated cellular PARylation is tightly controlled by (1) the PAR degrading enzyme PARG, as shown by PARylation accumulation in PDD-treated OLs, (2) PARP1 auto-PARylation, which provides negative feedback to PARP1 activity (Gupte et al., 2017), and (3) the downregulation of PARP1 itself in fully matured OLs. Interestingly, *in vivo* PARG inhibition increases the PAR signal in Sox10$^+$ OLCs but does not lead to massive

ectopic PAR accumulation in non-OLCs (Figure 5C), suggesting that PARG is activated in cells that simultaneously exhibit PARP1's PARylation activities, which are identified as OLCs (Figure 4).

The potential triggers for PARP1 activation in developing OLs remain unclear. DNA damage is the canonical activator for PARP1 (D'Amours et al., 1999). Excessive PARP1 hyperactivation by DNA damaging agents mediates neuronal death *in vitro* (Alano et al., 2010). However, PARP1 activity in OLs is unlikely triggered by DNA damage in the developing CNS where genomic DNA integrity is maintained. In this regard, PARP1 activation may play a minor role in OL death, which is supported by our data showing that PARP1 inhibition or depletion does not affect OL death in the developing CNS. Our finding is consistent with previous data that PARP1 depletion or inhibition does not affect primary OL death elicited by peroxynitrite (Scott et al., 2003). Furthermore, our data also suggest (Figure 7) that PARP1 activity is necessary for OL regeneration and dispensable for OL death, at least during remyelination. It remains to be determined whether PARP1 and its activity regulate OL death or survival under demyelinating conditions as previously reported (Veto et al., 2010). Our genetic model of tamoxifen-inducible cell-specific PARP1 deletion would be an appropriate tool to answer this question.

A potential role of PARP1 in regulating RNA metabolism and binding

Our results suggest a crucial role of PARP1 in regulating RNA binding and metabolism, which is consistent with an increasingly appreciated role of PARP1 in RNA biology (Ke et al., 2019). We focused on the target protein Myef2, which we reported to control OPC differentiation in part through PARylation-regulated myelin gene expression at the posttranscriptional level. We found that PARP1 binds to and PARylates Myef2 and that inhibiting PARP1 activity potentiates the association of Myef2 with myelin gene mRNAs, repressing myelin protein translation through yet unknown mechanisms. In support of this notion, our functional analysis revealed that *Myef2* knockdown promotes myelin protein expression at the posttranscriptional, but not mRNA, level in primary OLs and rescues 4HQ-mediated inhibition of myelin protein expression. These data suggest a working model in which PARP1 enzymatic activity promotes oligodendrogenesis by PARylating and releasing the inhibition of Myef2 on myelin protein expression (Figure 6I). It remains to be determined how Myef2 represses myelin protein expression and whether Myef2 plays a role in impeding OL regeneration under demyelination and remyelination conditions.

We reported that PARP1 inhibition decreased the mRNA level of myelin-associated proteins, but Myef2 inhibition did not. The different effects of PARP1 and Myef2 suggest that, in addition to posttranscriptional regulation of myelin gene expression through Myef2, PARP1 may regulate myelin gene expression at the transcriptional levels through other targets. For instance, Mecp2, which regulates myelin gene transcription (Sharma et al., 2015), and histone H1, which interacts with PARP1 at the promoter regions to regulate gene expression (Krishnakumar et al., 2008), may play a role in PARP1 regulation of myelin gene transcription.

Thyroid hormone receptor (THR)-mediated signaling is a crucial driver for OPC differentiation through controlling gene expression of differentiation-related factors

(Baldassarro et al., 2019; Billon et al., 2002; Dugas et al., 2012). Another intriguing candidate of PARP1 targets, the THR-associated protein Thrap3 (aka Trap150) (Table S3) is a component of the thyroid hormone (T3)-activated THR complex (Fondell et al., 1996), an essential transcription factor for OPC differentiation (Lee and Petratos, 2016). Thrap3 also participates in mRNA splicing (Heyd and Lynch, 2010; Lee et al., 2010) and circadian-rhythm-regulated gene expression (Lande-Diner et al., 2013), both of which modulate OPC differentiation and myelination (Huang et al., 2020; Wang et al., 2012; Xu et al., 2020). It is possible that PARP1 regulates OPC differentiation by PARylating and modulating Thrap3 function as well, thus affecting Thrap3-mediated gene transcription and mRNA metabolism. Future studies are warranted to define the functional association between PARP1 and Thrap3 and how the potential PARP1/Thrap3 axis regulates the expression of oligodendroglial differentiation-related factors.

Therapeutic potentials of PARP1 in demyelinating disorders

PARP1 expression and its activity were reported to be elevated in T and B lymphocytes (Meira et al., 2019), myeloid cells (Farez et al., 2009), and OLs, to a lesser extent, astrocytes and microglia/macrophages in the active brain lesions (Veto et al., 2010) of MS, an inflammatory demyelinating disease of the CNS. Pharmacological PARP1 inhibition was reported to protect against the immune activation and disease severity of experimental autoimmune encephalomyelitis (EAE), an animal model of MS (Cavone et al., 2011; Farez et al., 2009; Scott et al., 2004). However, genetic PARP1 deficiency was reported to worsen EAE disease severity (Kamboj et al., 2013; Selvaraj et al., 2009) and had no effect on pro-inflammatory gene expression in the spinal cord (Selvaraj et al., 2009), which is consistent with the unaltered expression of proinflammatory cytokines in microglia/macrophages (CD11b^{+}) isolated from the spinal cord of *Parp1*-deficient EAE mice (Farez et al., 2009). While the reason for the conflicting conclusions is likely multifaceted, non-cellular specificity and potential "off-target" effects of PARP1 inhibitors cannot be neglected. Notably, the PARP1 inhibitors used in previous EAE studies (PJ34, PHE, and 5AIQ) have been shown to target not only a broader range of the 17 PARP members (Wahlberg et al., 2012) but also off-target pathways such as the inflammation modulators metalloproteinase 9 (MMP9) (Mishra and Kowluru, 2017; Tao et al., 2015) and MMP2 (Nicolescu et al., 2009), PIM serine/threonine kinase family proteins PIM1/PIM2 (Antolín et al., 2012), and likely P2Y12 receptor signaling (Lechaftois et al., 2014). The conflicting observations suggest that PARP1 may play a cell-type-dependent role in regulating neuroinflammation, neuronal/axonal degeneration, and oligodendrogliopathy, three major pathological components cooperatively determining the MS disease course and neurological progression. Hence, it is important to employ cell-specific and/or time-conditional PARP1 deletion paradigms to interrogate the therapeutic value of PARP1 in neuroinflammation, neuropathy, and oligodendrogliopathy of MS animal models.

Our study suggests that PARP1 promotes remyelination in the CPZ model, which mimics pattern III MS lesions of primary oligodendrogliopathy. Our results also indicate that PARP1 plays a minor role in OL death, a conclusion which seems contradictory with previous data reporting that PARP1 inhibition protects OLs from CPZ-induced death (Veto et al., 2010). However, the time-course analysis showed that PARP1 was activated primarily in

CD68^{+} activated microglia (Figure 7D) and minimally in Sox10^{+} oligodendroglia (Figure 7C) during CPZ-induced demyelination stages. We hypothesize that PARP1 chemical inhibition during CPZ diet maintenance (Veto et al., 2010) dampens microglial activation, which indirectly protects OLs and myelin against CPZ-induced damage. Supporting this hypothesis, PARP1 inhibition has been reported to impair microglial activation in response to various stimuli (Kauppinen et al., 2011; Kauppinen and Swanson, 2005; Stoica et al., 2014). Notably, microglial activation is not only necessary but also sufficient for OL death and myelin damage in CPZ model (Marzan et al., 2021). Future studies employing OL-specific PARP1 depletion are needed to prove or falsify this hypothesis.

PARP1 has been proposed to induce neuronal cell death in ischemic and traumatic brain damage (Komjáti et al., 2005; Moroni, 2008). The effect of PARP1 on neuronal cell death/survival seems to depend on the injury severity, as PARP1 inhibition could enhance or prevent primary cortical neuron death, depending on the severity of oxidative stress elicited by H_2O_2 incubation (Diaz-Hernandez et al., 2007). PARP1 activation was shown to be neuroprotective against oxidative neuron injury *in vivo*, elicited by disrupting the homeostasis of endogenous antioxidant glutathione (Diaz-Hernandez et al., 2007), which better reflects the mild but chronic pathophysiological contexts of MS (Carvalho et al., 2014) and neurodegenerative disorders (Johnson et al., 2012). Hence, more studies are needed to define the role of PARP1 in neuron death and survival in the setting of inflammatory demyelination EAE models. The genetic mouse tools generated in this study will help solve these puzzles.

STAR★METHODS

RESOURCE AVAILABILITY

Lead contact—Further information and requests may be directed to and will be fulfilled by the Lead Contact Fuzheng Guo (fzguo@ucdavis.edu).

Materials availability—All requests for resources and reagents should be directed to and will be fulfilled by the Lead Contact author. All reagents will be made available on request after completion of a Materials Transfer Agreement.

Data and code availability—Bulk brain RNA-seq data have been deposited at GEO and are publicly available as of the date of publication. Accession numbers are listed in the Key resources table. Original western blot images have been deposited at Mendeley and are publicly available as of the data of publication. The DOI is listed in the Key resources table. Microscopy data reported in this paper will be shared by the lead contact upon request.

EXPERIMENTAL MODEL AND SUBJECT DETAILS

Generation of Parp1 KO and cKO mice—Parp1-floxed mice were provided by Dr. Kraus (Luo et al., 2017) via an approved Material Transfer Agreement (MTA). *Olig2-Cre* (B6.129-*Olig2^{tm1.1(cre)Wdr}*/J, stock 025567), *Pdgfra-CreER^{T2}* (B6N.Cg-*Tg(Pdgfra-cre/ERT)467Dbe*/J, stock 018280) and *Rosa26-LoxP-STOP-LoxP-*EYFP (referred to as *Rosa26-EYFP*, B6.129X1-*Gt(ROSA)26Sor^{tm1(EYFP)Cos}*/J, stock 006148) were purchased from the

Jackson Laboratory. Cre transgene was always maintained as heterozygosity. We crossed *Cre* lines with *Parp1*$^{fl/fl}$ mice to generate *Parp1* cKO mice. Mice that are homozygous for *Parp1* KO were purchased from the Jackson Laboratory (129S-*Parp1*^{tm1Zqw}/J, stock 002779) and bred with C57BL/6J mice (stock 002779, Jackson Laboratory) to get heterozygous *Parp1* KO mice. WT and *Parp1* KO mice were subsequently generated by crossing female heterozygous *Parp1* KO mice with male heterozygous *Parp1* KO mice. Both male and female mice were used in this study. All animals were from C57BL/6 background and maintained in 12 h light/dark cycle with water and food. Animals and procedures in this study were approved by the Institutional Animal Care and Use Committee at the University of California, Davis.

Mouse studies, 4HQ or PDD injections and cuprizone model—For *Pdgfra-CreER*^{T2}:*Parp1*$^{fl/fl}$ and littermate controls, tamoxifen was dissolved in a mixture of ethanol and sunflower seed oil (1:9, v/v) at the concentration of 30 mg/ml. Tamoxifen was administered subcutaneously to neonatal pups on P1, P2, and P3 daily at a dose of 10 μL (300 μg) once a day and mice were euthanized at P9 for OL differentiation assay according to our previous protocols (Zhang et al., 2018b, 2021a, 2021b), or administrated on P6 and P7 at a dose of 20 μL (600 μg) once a day and mice were euthanized at P14 for myelination assay. For PARylation study, neonatal mice were injected with PARP inhibitor 4-hydroxyquinazoline (4HQ) 100 mg/kg body weight, or PARG inhibitor PDD 00017273 (PDD) 10 g/kg body weight or vehicle control subcutaneously from postnatal day 2 (P2) to P10, and euthanized for analysis 2 h after the last injection. For postnatal studies, the day when pups were born was designated as P0. Experimental demyelination was induced by feeding 8-week-old male mice with 0.2% cuprizone diet. After 6 weeks of treatment, cuprizone feedings were discontinued and changed to a regular diet for 1 week (6+1 W) or 6 weeks (6+6 W) for remyelination. To study the effect on remyelination, 4HQ (100 mg/kg) or DMSO vehicle were intraperitoneally injected into wild-type mice daily from day 1 through day 7, or tamoxifen was injected intraperitoneally into *Pdgfra-CreER*^{T2}:*Parp1*$^{fl/fl}$ and littermate control mice from day 1 to day 5, after returning to normal diet, and mice were euthanized at weeks 7 (6+1 W) for further analysis. Both male and female mice were used in these studies.

Mice OPCs primary culture, differentiation, and treatment—Primary OPCs were isolated from cerebral cortices of P0 to P2 mice using immune-panning procedure according to our previous protocol (Zhang et al., 2018b, 2020, 2021a, 2021b). Cerebral cortices from male and female pups were combined. After stripping the meninges, cerebral cortices were enzymatically digested using papain (20 U/ml, Worthington) supplemented with DNase I (250 U/ml, Sigma) and D-(+)-glucose (0.36%, AMRESCO) for 1 h at 37°C, and mechanically triturated to obtain single cell. The cell suspension was centrifuged, resuspended in DMEM medium with 10% heat-inactivated fetal bovine serum and penicillin/streptomycin, and plated on poly-D-lysine (PDL, Millipore) coated 10 cm dishes. After 24 h incubation, cells were washed using HBSS, and cultured in serum-free growth medium (GM), containing 30% of B104–1-1 neuroblastoma medium and 70% of N1 medium (DMEM with 5 mg/ml insulin (Sigma), 50 μg/ml apo-transferrin (Sigma), 100 μM putrescine (Sigma), 30 nM Sodium selenite (Sigma), 20 nM progesterone (Sigma) until

80% of confluency. The mixed glial cells were then dissociated in single cell suspension, incubated on Thy1.2 (CD90.2) antibody (10 μl, Biolegend) coated Petri-dish to deplete astrocytes, neurons and meningeal cells and then seeded on NG2 antibody (5 μl, Millipore) coated Petri-dish to select OPCs. The isolated OPCs were then cultured on PDL-coated plates using GM plus 5 ng/ml FGF (Peprotech), 4 ng/ml PDGF-AA (Peprotech), 50 μM Forskolin (Peprotech,) and glutamax (Thermo Fisher). To induce differentiation, OPCs were cultured in the differentiation medium (DM), consisting of F12/high-glucose DMEM plus 12.5 μg/ml insulin, 100 μM Putrescine, 24 nM Sodium selenite, 10 nM Progesterone, 10 ng/ml Biotin, 50 μg/ml Transferrin (Sigma), 30 ng/ml 3,3′,5-Triiodo-L-thyronine (Sigma), 40 ng/ml L-Thyroxine (Sigma), glutamax and P/S. OPCs with 80% confluence were treated with 10 μM 4HQ, 1 μM PDD or vehicle control in the DM medium. OPCs differentiation was analyzed at the time points indicated in Figures 4H and 5H. OPCs from WT and *Parp1* KO mice were isolated, cultured until 80% confluence and differentiated for 1, 3 and 4 days in DM medium. Cells are cultured at 37°C in a humidified atmosphere with 5% CO_2.

Rat OPC primary culture, differentiation, and loss-of-function—Primary mixed glial cells were prepared from P0-P2 rat cerebral cortices as previously described (Zhang et al., 2020, 2021a). Mixed glial cells were plated on PDL-coated T75 flasks in high glucose DMEM medium supplemented with 10% heat-inactivated fetal bovine serum and 1% Penicillin/Streptomycin. Medium was changed every 2 days until astrocytes are confluent. Flasks were shaken for 1 h at 37°C and 200 rpm on an orbital shaker (Cat# C491, Hanchen) to remove microglia. After wash with PBS, 20 mL 10% FBS/DMEM was added into each flask, followed by shaking for 6 h at 37°C and 200 rpm to get OPCs. OPCs were seeded on PDL-coated plates in GM for further study. Double-stranded *Parg, Myef2* or universal negative control small interfering RNAs (siRNA) were purchased from Sigma-Aldrich. Primary OPCs growing on 6-well plates at 80% confluency were transfected with a concentration of 25 nM siRNA and 9 μL HiPerFect transfection reagent (QIAGEN) in the differentiation medium. Cells were incubated with the medium containing siRNA at the time points indicated in Figures 5O and 6J. Cells were processed for differentiation analysis after transfection. Cells are cultured at 37°C in a humidified atmosphere with 5% CO_2.

METHOD DETAILS

Tissue preparation and immunohistochemistry (IHC)—Tissue preparation and IHC were conducted as previously described (Zhang et al., 2021a). After anesthetization by ketamine/xylazine mixture, mice were transcardially perfused with ice-cold PBS. Tissues were collected, and immediately placed on dry ice for protein or RNA extraction or fixed in fresh 4% paraformaldehyde (PFA, Electron Microscopy Science) for histological study. After post-fix in 4% PFA for 2 h at room temperature (RT), tissues were washed with PBS three times, 15 min each time, cryopreserved in 30% sucrose (Fisher Chemical) in PBS overnight at 4°C and embedded in O.C.T. (VWR International). Serial coronal sections (12 μm) were cut by a Leica Cryostat (CM 1900–3-1) and stored in 80°C. IHC was conducted as below: slices were air dry at RT for 2 h, and blocked with 10% donkey serum in 0.1% Triton X-100/PBS (v/v) for 1 h at RT, followed by incubation with primary antibodies overnight at 4°C. After wash with PBST (PBS with 0.1% Tween-20, v/v), slices were incubated with fluorescence conjugated secondary antibodies for 2h at RT. DAPI was applied as

nuclear counterstain. All images shown were obtained by Nikon A1 confocal microscope. 10 μm of optical thickness sections were obtained by confocal z stacking (step size 1 μm) and projected into one flattened image for quantification. The following antibodies were used in IHC: PARP1 (1:100, Active Motif; 1:100, Proteintech), Anti-poly-ADP-ribose binding reagent (1:100, Millipore), Sox2 (1:500, Santa Cruz Biotechnology), CC1 (1:200, Calbiochem), TCF7l2 (1:100, Cell Signaling Technology; 1:100, Millipore), PDGFRα (1:100, R&D System), EYFP (1:200, Millipore), Sox10 (1:100, Abcam), MBP (1:100, Novus), Myef2 (1:100, Proteintech), SMI312 (1:100, BioLegend), Iba1 (1:100, Novus), GFAP (1:100, Millipore). All secondary antibodies Alexa Fluor® 488- or Alexa Fluor 594-conjugated AffiniPure F(ab')$_2$ fragments (1:500) were from Jackson ImmunoResearch Laboratories.

Black-Gold II myelin staining—Black-Gold II myelin stain (Millipore) was performed according to the manufacturer's instruction. The fixed, frozen sections (12 um) were incubated with 0.3% Black-Gold II stain for 20 min at 60°C. The stain was fixed with 1% sodium thiosulfate solution, and then washed, dehydrated using a series of gradated alcohol (50%, 75%, 85%, 95% and 100%), cleared in xylene, and coverslipped with mounting medium (Fisher Scientific). Staining was visualized using an Olympus BX61 microscope and quantified by ImageJ software.

Toluidine blue staining and transmission electron microscopy (TEM)—Mice were anesthetized with ketamine/xylazine mixture and perfused with 4% PFA, followed by 3% glutaraldehyde (Electron Microscopy Science, dilute in PBS, pH 7.4) at a speed of 5 mL per minute. Spinal cord was carefully dissected out and fixed with 3% glutaraldehyde overnight, followed by wash with 0.2 M sodium cacodylate buffer (pH 7.2, Electron Microscopy Science) twice, 10 min each time, post-fixed with 2% (w/v) aqueous osmium tetroxide (Electron Microscopy Science) for 2 h and washed with sodium cacodylate twice, 10 min each time. The resulting spinal cord was then dehydrated with 50, 70, 90, and 100% ethanol, followed by wash in propylene oxide three times, 30 min each time, and incubation with 1:1 mixture of Propylene Oxide:Eponate Resin (Electron Microscopy Science) overnight, and with 1:3 mixture of Propylene Oxide:Eponate Resin for 10 h, and with 100% Eponate Resin overnight. The resulting specimens were embedded in EMBed-812 Resin for 2 days at 65°C. Semithin (500 nm) sections were cut by using a Leica EM UC6 microtome and then incubated with 2% toluidine blue (Ted Pella Inc.) at 100°C for 2 min, followed by imaging on Olympus BX61 microscope. Ultrathin (70 – 80 nm) sections were cut on a Leica EM UC7 microtome and collected on 1 mm Formvar-coated copper slot grids, double stained with uranyl acetate and lead citrate, followed by imaging on a CM120 electron microscope.

Immunocytochemistry (ICC)—Cells cultured on glass slides were fixed in 4% PFA for 30 min, permeabilized with 0.1% Triton X-100 in PBS and blocked with 10% donkey serum. The cells were then washed with PBS and incubated with Primary antibodies overnight at 4°C, followed by fluorescence-conjugated secondary antibodies (1:200) for 2 h at room temperature. Nuclei were visualized using DAPI. Fluorescent images were observed

with Nikon A1 confocal microscope. Intensity of MBP fluorescence were quantified using ImageJ software.

Cell viability assay—Cells were seeded in 48-well plates at a density of 1×10^5 cells/mL and cultured for 24 h before further treatment. 200 μL of MTT solution (5 mg/mL, diluted in PBS) was added to each well and incubated at 37°C for 4 h. The medium was removed and 200 μL of DMSO was added to each well to dissolve formazan crystals. Optical densities (OD) were determined by a microplate reader (SpectraMax i3x, Molecular Devices) at 570 nm and 650 nm. Cell viability was expressed as a percentage with the control cells, which was taken as 100%.

Protein extraction and western blot assay—Tissue or cells were lysed in N-PER Neuronal Protein Extraction Reagent (Thermo Fisher) supplemented with protease and phosphatase inhibitor cocktail (Thermo Fisher) and PMSF (Cell Signaling Technology). After incubation on ice for 10 min and centrifugation at $10,000 \times g$ for 10 min at 4°C, the concentrations of each sample were measured using BCA protein assay kit (Thermo Fisher Scientific). Equal volumes (30 μg) of cell lysates from each condition were resolved by AnykD Mini-PROTEAN TGX precast gels (BIO-RAD) or 7.5% Mini-PROTEAN TGX precast gels (BIO-RAD). The proteins were transferred onto 0.2 μm nitrocellulose membrane (BIO-RAD) using Trans-blot Turbo Transfer system (BIO-RAD). After blocking with 5% BSA (Cell signaling) for 1 h at room temperature, the membranes were incubated with primary antibodies overnight at 4 °C, followed by suitable HRP-conjugated secondary antibodies. Proteins of interest were visualized by Western Lightening Plus ECL (Perkin Elmer). NIH ImageJ was used to analyze protein levels. Primary and secondary antibodies used were: PARP1 (1:1000, Active Motif), Anti-poly-ADP-ribose binding reagent (1:1000, Millipore), Sox2 (1:1000, Santa Cruz Biotechnology), TCF7l2 (1:100, Cell Signaling Technology; 1:100, Millipore), Myef2 (1:100, Proteintech), MBP (1:100, Novus), MAG (1:1000, Millipore), PLP (1:1000, Thermo Fisher Scientific), TLE3 (1:1000, Proteintech), AIF (1:1000, Abcam), Gasdermin D (1:1000, Cell Signaling Technology), MLKL (1:1000, Proteintech), p-MLKL (S345) (1:1000, Cell Signaling Technology), β-actin (1:1000, Cell Signaling Technology), and HRP goat anti-rabbit (1:3000, Thermo Fisher Scientific), anti-mouse (1:3000, Thermo Fisher Scientific) or anti-rat (1:3000, Cell Signaling Technology) secondary antibodies.

Co-immunoprecipitation (Co-IP)—For western blotting assay, Co-IP was performed with Pierce Crosslink Magnetic IP/Co-IP kit (Thermo Fisher) following the manufacturer's instructions. 10 mg of primary antibodies or isotype control IgG were covalently cross-linked to 25 μL of protein A/G magnetic beads (Thermo Fisher). Proteins were extracted with the Pierce IP Lysis/Wash Buffer (Thermo Fisher) supplemented with PMSF (Cell Signaling Technology) and protease and phosphatase inhibitor cocktail (Thermo Fisher). A portion of each sample was saved as input. An equal amount (1 mg) of each protein extract was incubated with protein A/G magnetic beads cross-linked with primary antibodies or isotype control IgG overnight at 4°C. The beads were then washed to remove non-bound material and protein was eluted in a low-PH elution buffer that dissociates bound antigen from the antibody-crosslinked beads. The elute was then added with Neutralization buffer

to neutralize the low PH and Lane marker sample buffer containing β-mercaptoethanol for SDS-PAGE and western blotting. Primary antibodies and isotype control IgG used were: PARP1 (Active Motif), PAR (Trevigen), Sox2 (Santa Cruz Biotechnology), Myef2 (Proteintech), Normal rabbit IgG (Cell Signaling Technology) and Normal goat IgG (R&D Systems).

For LC-MS/MS assay, Co-IP was performed with Pierce Classic Magnetic IP/Co-IP kit (Thermo Fisher) according to manufacturer's instructions. 1 mg of protein lysate was incubated with 10 μg of primary antibodies or isotype control IgG overnight at 4°C. Pierce Protein A/G Magnetic Beads were washed three times using Pierce IP Lysis/Wash Buffer for LC-MS/MS analysis.

LC-MS/MS—For protein digestion, samples on magnetic beads were washed four times with 200 ul of 50mM ammonium bicarbonate (AMBIC) with a 20 min shake time at 4°C. 2.5 ug of trypsin gold (Mass spectrometry grade, V528A, Promega) was added to the beads and samples were digested overnight at 800 rpm shake speed at RT. After overnight digestion, the peptide extracts were reduced in volume by vacuum centrifugation and a small portion of the extract was used for fluorometric peptide quantification (Thermo scientific Pierce). Samples were analyzed for LC-MS/MS analysis by UC Davis Proteomics core. One microgram of sample based on the fluorometric peptide assay was loaded for each LC-MS/MS on a Thermo Scientific Q Exactive Plus Orbitrap Mass spectrometer in conjunction Proxeon Easy-nLC II HPLC (Thermo Scientific) and Proxeon nanospray source. Tandem mass spectra were extracted and charge state deconvoluted by Proteome Discoverer (Thermo Scientific). All MS/MS samples were analyzed using X! Tandem (The GPM, thegpm.org; version X! Tandem Alanine (2017.2.1.4)). Scaffold (version Scaffold_4.8.4, Proteome Software Inc., Portland, OR) was used to validate MS/MS based peptide and protein identifications.

RNA extraction and quantitative real-time PCR (qRT-PCR)—RNA isolation was performed using the RNeasy Lipid Tissue Mini Kit (QIAGEN) with RNase-Free DNase Set (QIAGEN) to remove genomic DNA. RNA concentration was measured by Nanodrop 2000 Spectrophotometer (Thermo Fisher Scientific). cDNA was synthesized by QIAGEN Omniscript RT Kit (QIAGEN). RT-qPCR was performed using QuantiTect SYBR® Green PCR Kit (QIAGEN) on Agilent MP3005P thermocycler. For quantification, the mRNA expression level of interested genes in each sample was normalized to that of the internal control gene Hsp90, and fold change in gene expression was calculated based on the Equation $2^{\wedge}(Ct(\text{cycle threshold}) \text{ of } Hsp90 - Ct \text{ of indicated genes})$. The gene expression levels in control groups were normalized to 1. Please see Table S5 for primer sequences.

RNA-sequencing (RNA-seq) and bioinformatic analysis—Total RNA was prepared from forebrains of *Pdgfra-CreER^{T2} Parp1^{fl/fl}* mice (n = 3) and controls (n = 3) using QIAGEN RNeasy for lipid tissues with on-column DNase I digestion. The quality of RNA samples was determined by the Bioanalyzer 2100 system (Agilent Technologies). The RNA integrity number (RIN) of all our RNA samples used for RNA-seq and qPCR was greater than 6.8. The cDNA library was prepared using the NEBNext Ultra Directional RNA Library Prep Kit (New England BioLabs) for sequenced on the Illumina HiSeq 4000

sequencing platform. Paired-end clean reads were aligned to the reference genome (mouse genome mm10) using STAR version2.5 (Spliced Transcripts Alignment to a Reference). HTseq v0.6.1 was used to count the read numbers mapped of each gene and FPKM was calculated to indicate the gene expression level. Differentially expressed genes (DEGs) were analyzed using DESeq version 2.1.6.3 and adjusted P value *padj* < 0.05 was assigned as DEGs. Gene ontology (GO) enrichment analysis of DEGs was performed using the National Institutes of Health online tool DAVID (https://david.ncifcrf.gov/). GO terms with adjusted *p* value less than 0.05 were considered significantly enriched.

RNA immunoprecipitation (RIP)—RIP was conducted as reported. D2 OLs were lysed in Pierce IP Lysis/Wash Buffer supplemented with protease inhibitor (Cell Signaling Technology) and 100 U/ml RNaseOUT (Thermo Fisher) for 30 min on ice. After centrifugation, the protein lysate was incubated with 10 μg of Myef2 antibody, or normal rabbit IgG overnight at 4°C. 50 μL of protein G Dynabeads (Life Technologies) were added to the lysate and antibody mix and incubated for 2 h at 4°C. The beads were then washed five times using 1 mL of lysis buffer. RNA binding to Myef2 protein and 10% of the input lysate were extracted by Buffer RLT supplemented with β-mercaptoethanol (10 μL per 1 mL Buffer RLT) and vortexed to mix. 1 volume of 70% ethanol was added to the homogenized lysate, and sample was transferred to RNeasy Mini spin column, centrifuged and washed with Buffer RW1 and Buffer RPE. RNA was eluted by 25 μL of RNase-free water. Purified RNA was then analyzed by RT-qPCR.

Rotarod test—Accelerating rotarod test was used for motor function assessment. The starting speed of rotarod was 4 rotations per minute (rpm) and the maximal speed was 40 rpm with 1.2 rpm incremental every 10 s. Mice were trained for two consecutive days (4 trials each day with 60 min interval between trials) followed by data collection on the third day. The retention time of each mouse on rod was recorded and calculated by averaging 3 individual trials.

QUANTIFICATION AND STATISTICAL ANALYSIS

Quantification was performed by observers blind to genotype and treatment. Data were presented as mean ± s.e.m. in the study. Scatter dot plots were used to quantify data throughout our manuscript. Each dot in the scatter dot plots represents one mouse or one independent experiment. Shapiro-Wilk approach was used for testing data normality. Unpaired two-tailed Student's t test was used for statistically analyzing two groups of data and degree of freedom (df) were presented as $t_{(df)}$ in figure legends. One-way ANOVA followed by Tukey's post-test was used for statistically analyzing three or more groups of data. The F ratio, and DFn and DFd was presented as $F_{(DFn, DFd)}$ in the figure legends where DFn stands for degree of freedom numerator and DFd for degree of freedom of denominator. All data graphing and statistical analyses were performed using GraphPad Prism version 8.0. *P* value less than 0.05 was considered as significant. ns stands for not significant with *P* value greater than 0.05. See Table S4 for detailed statistical information in the main figures

Supplementary Material

Refer to Web version on PubMed Central for supplementary material.

REFERENCES

Abaza I, and Gebauer F (2008). Trading translation with RNA-binding proteins. RNA 14, 404–409. [PubMed: 18212021]

Alano CC, Garnier P, Ying W, Higashi Y, Kauppinen TM, and Swanson RA (2010). NAD+ depletion is necessary and sufficient for poly(ADP-ribose) polymerase-1-mediated neuronal death. J. Neurosci. 30, 2967–2978. [PubMed: 20181594]

Antolín AA, Jalencas X, Yélamos J, and Mestres J (2012). Identification of pim kinases as novel targets for PJ34 with confounding effects in PARP biology. ACS Chem. Biol. 7, 1962–1967. [PubMed: 23025350]

Baldassarro VA, Marchesini A, Giardino L, and Calzá L (2017). PARP activity and inhibition in fetal and adult oligodendrocyte precursor cells: Effect on cell survival and differentiation. Stem Cell Res. (Amst.) 22, 54–60.

Baldassarro VA, Krȩ el W, Fernández M, Schuhbaur B, Giardino L, and Calzá L (2019). The role of nuclear receptors in the differentiation of oligodendrocyte precursor cells derived from fetal and adult neural stem cells. Stem Cell Res. (Amst.) 37, 101443.

Billon N, Jolicoeur C, Tokumoto Y, Vennström B, and Raff M (2002). Normal timing of oligodendrocyte development depends on thyroid hormone receptor alpha 1 (TRalpha1). EMBO J. 21, 6452–6460. [PubMed: 12456652]

Carvalho AN, Lim JL, Nijland PG, Witte ME, and Van Horssen J (2014). Glutathione in multiple sclerosis: more than just an antioxidant? Mult. Scler. 20, 1425–1431. [PubMed: 24842957]

Cavone L, and Chiarugi A (2012). Targeting poly(ADP-ribose) polymerase-1 as a promising approach for immunomodulation in multiple sclerosis? Trends Mol. Med. 18, 92–100. [PubMed: 22078487]

Cavone L, Aldinucci A, Ballerini C, Biagioli T, Moroni F, and Chiarugi A (2011). PARP-1 inhibition prevents CNS migration of dendritic cells during EAE, suppressing the encephalitogenic response and relapse severity. Mult. Scler. 17, 794–807. [PubMed: 21343230]

Chavali M, Ulloa-Navas MJ, Pérez-Borredá P, Garcia-Verdugo JM, McQuillen PS, Huang EJ, and Rowitch DH (2020). Wnt-Dependent Oligodendroglial-Endothelial Interactions Regulate White Matter Vascularization and Attenuate Injury. Neuron 108, 1130–1145.e5. [PubMed: 33086038]

D'Amours D, Desnoyers S, D'Silva I, and Poirier GG (1999). Poly(ADP-ribosyl)ation reactions in the regulation of nuclear functions. Biochem. J. 342, 249–268. [PubMed: 10455009]

Davidovic L, Vodenicharov M, Affar EB, and Poirier GG (2001). Importance of poly(ADP-ribose) glycohydrolase in the control of poly(ADP-ribose) metabolism. Exp. Cell Res. 268, 7–13. [PubMed: 11461113]

Diaz-Hernandez JI, Moncada S, Bolaños JP, and Almeida A (2007). Poly(ADP-ribose) polymerase-1 protects neurons against apoptosis induced by oxidative stress. Cell Death Differ. 14, 1211–1221. [PubMed: 17347665]

Dugas JC, Ibrahim A, and Barres BA (2012). The T3-induced gene KLF9 regulates oligodendrocyte differentiation and myelin regeneration. Mol. Cell. Neurosci. 50, 45–57. [PubMed: 22472204]

Fancy SP, Baranzini SE, Zhao C, Yuk DI, Irvine KA, Kaing S, Sanai N, Franklin RJ, and Rowitch DH (2009). Dysregulation of the Wnt pathway inhibits timely myelination and remyelination in the mammalian CNS. Genes Dev. 23, 1571–1585. [PubMed: 19515974]

Fancy SP, Harrington EP, Baranzini SE, Silbereis JC, Shiow LR, Yuen TJ, Huang EJ, Lomvardas S, and Rowitch DH (2014). Parallel states of pathological Wnt signaling in neonatal brain injury and colon cancer. Nat. Neurosci. 17, 506–512. [PubMed: 24609463]

Farez MF, Quintana FJ, Gandhi R, Izquierdo G, Lucas M, and Weiner HL (2009). Toll-like receptor 2 and poly(ADP-ribose) polymerase 1 promote central nervous system neuroinflammation in progressive EAE. Nat. Immunol. 10, 958–964. [PubMed: 19684606]

Fondell JD, Ge H, and Roeder RG (1996). Ligand induction of a transcriptionally active thyroid hormone receptor coactivator complex. Proc. Natl. Acad. Sci. USA 93, 8329–8333. [PubMed: 8710870]

Giampetruzzi A, Carson JH, and Barbarese E (2013). FMRP and myelin protein expression in oligodendrocytes. Mol. Cell. Neurosci. 56, 333–341. [PubMed: 23891804]

Gupte R, Liu Z, and Kraus WL (2017). PARPs and ADP-ribosylation: recent advances linking molecular functions to biological outcomes. Genes Dev. 31, 101–126. [PubMed: 28202539]

Guzman KM, Brink LE, Rodriguez-Bey G, Bodnar RJ, Kuang L, Xing B, Sullivan M, Park HJ, Koppes E, Zhu H, et al. (2020). Conditional depletion of Fus in oligodendrocytes leads to motor hyperactivity and increased myelin deposition associated with Akt and cholesterol activation. Glia 68, 2040–2056. [PubMed: 32187401]

Hammond E, Lang J, Maeda Y, Pleasure D, Angus-Hill M, Xu J, Horiuchi M, Deng W, and Guo F (2015). The Wnt effector transcription factor 7-like 2 positively regulates oligodendrocyte differentiation in a manner independent of Wnt/b-catenin signaling. J. Neurosci. 35, 5007–5022. [PubMed: 25810530]

Hassa PO (2009). The molecular "Jekyll and Hyde" duality of PARP1 in cell death and cell survival. Front. Biosci. 14, 72–111.

He D, Wang J, Lu Y, Deng Y, Zhao C, Xu L, Chen Y, Hu YC, Zhou W, and Lu QR (2017). lncRNA Functional Networks in Oligodendrocytes Reveal Stage-Specific Myelination Control by an lncOL1/Suz12 Complex in the CNS. Neuron 93, 362–378. [PubMed: 28041882]

Heyd F, and Lynch KW (2010). Phosphorylation-dependent regulation of PSF by GSK3 controls CD45 alternative splicing. Mol. Cell 40, 126–137. [PubMed: 20932480]

Huang S, Choi MH, Huang H, Wang X, Chang YC, and Kim JY (2020). Demyelination Regulates the Circadian Transcription Factor BMAL1 to Signal Adult Neural Stem Cells to Initiate Oligodendrogenesis. Cell Rep. 33, 108394. [PubMed: 33207207]

James DI, Smith KM, Jordan AM, Fairweather EE, Griffiths LA, Hamilton NS, Hitchin JR, Hutton CP, Jones S, Kelly P, et al. (2016). First-in-Class Chemical Probes against Poly(ADP-ribose) Glycohydrolase (PARG) Inhibit DNA Repair with Differential Pharmacology to Olaparib. ACS Chem. Biol. 11, 3179–3190. [PubMed: 27689388]

Johnson WM, Wilson-Delfosse AL, and Mieyal JJ (2012). Dysregulation of glutathione homeostasis in neurodegenerative diseases. Nutrients 4, 1399–1440. [PubMed: 23201762]

Kamaletdinova T, Fanaei-Kahrani Z, and Wang ZQ (2019). The Enigmatic Function of PARP1: From PARylation Activity to PAR Readers. Cells 8, 1625.

Kamboj A, Lu P, Cossoy MB, Stobart JL, Dolhun BA, Kauppinen TM, de Murcia G, and Anderson CM (2013). Poly(ADP-ribose) polymerase 2 contributes to neuroinflammation and neurological dysfunction in mouse experimental autoimmune encephalomyelitis. J. Neuroinflammation 10, 49. [PubMed: 23607899]

Kauppinen TM, and Swanson RA (2005). Poly(ADP-ribose) polymerase-1 promotes microglial activation, proliferation, and matrix metalloproteinase-9-mediated neuron death. J. Immunol. 174, 2288–2296. [PubMed: 15699164]

Kauppinen TM, Suh SW, Higashi Y, Berman AE, Escartin C, Won SJ, Wang C, Cho SH, Gan L, and Swanson RA (2011). Poly(ADP-ribose)polymerase-1 modulates microglial responses to amyloid b. J. Neuroinflammation 8, 152. [PubMed: 22051244]

Ke Y, Zhang J, Lv X, Zeng X, and Ba X (2019). Novel insights into PARPs in gene expression: regulation of RNA metabolism. Cell. Mol. Life Sci. 76, 3283–3299. [PubMed: 31055645]

Kessaris N, Fogarty M, Iannarelli P, Grist M, Wegner M, and Richardson WD (2006). Competing waves of oligodendrocytes in the forebrain and postnatal elimination of an embryonic lineage. Nat. Neurosci. 9, 173–179. [PubMed: 16388308]

Komjáti K, Besson VC, and Szabó C (2005). Poly (adp-ribose) polymerase inhibitors as potential therapeutic agents in stroke and neurotrauma. Curr. Drug Targets CNS Neurol. Disord. 4, 179–194. [PubMed: 15857303]

Krishnakumar R, Gamble MJ, Frizzell KM, Berrocal JG, Kininis M, and Kraus WL (2008). Reciprocal binding of PARP-1 and histone H1 at promoters specifies transcriptional outcomes. Science 319, 819–821. [PubMed: 18258916]

Kuhn PL, Petroulakis E, Zazanis GA, and McKinnon RD (1995). Motor function analysis of myelin mutant mice using a rotarod. Int. J. Dev. Neurosci. 13, 715–722. [PubMed: 8787862]

Lande-Diner L, Boyault C, Kim JY, and Weitz CJ (2013). A positive feedback loop links circadian clock factor CLOCK-BMAL1 to the basic transcriptional machinery. Proc. Natl. Acad. Sci. USA 110, 16021–16026. [PubMed: 24043798]

Lang J, Maeda Y, Bannerman P, Xu J, Horiuchi M, Pleasure D, and Guo F (2013). Adenomatous polyposis coli regulates oligodendroglial development. J. Neurosci. 33, 3113–3130. [PubMed: 23407966]

Lechaftois M, Dreano E, Palmier B, Margaill I, Marchand-Leroux C, Bachelot-Loza C, and Lerouet D (2014). Another "string to the bow" of PJ34, a potent poly(ADP-Ribose)polymerase inhibitor: an antiplatelet effect through P2Y12 antagonism? PLoS ONE 9, e110776. [PubMed: 25329809]

Lee JY, and Petratos S (2016). Thyroid Hormone Signaling in Oligodendrocytes: from Extracellular Transport to Intracellular Signal. Mol. Neurobiol. 53, 6568–6583. [PubMed: 27427390]

Lee KM, Hsu IaW., and Tarn WY (2010). TRAP150 activates pre-mRNA splicing and promotes nuclear mRNA degradation. Nucleic Acids Res. 38, 3340–3350. [PubMed: 20123736]

Luo X, and Kraus WL (2012). On PAR with PARP: cellular stress signaling through poly(ADP-ribose) and PARP-1. Genes Dev. 26, 417–432. [PubMed: 22391446]

Luo X, Ryu KW, Kim DS, Nandu T, Medina CJ, Gupte R, Gibson BA, Soccio RE, Yu Y, Gupta RK, and Kraus WL (2017). PARP-1 Controls the Adipogenic Transcriptional Program by PARylating C/EBPβ and Modulating Its Transcriptional Activity. Mol. Cell 65, 260–271. [PubMed: 28107648]

Marques S, Zeisel A, Codeluppi S, van Bruggen D, Mendanha Falcão A, Xiao L, Li H, Häring M, Hochgerner H, Romanov RA, et al. (2016). Oligodendrocyte heterogeneity in the mouse juvenile and adult central nervous system. Science 352, 1326–1329. [PubMed: 27284195]

Marzan DE, Brügger-Verdon V, West BL, Liddelow S, Samanta J, and Salzer JL (2021). Activated microglia drive demyelination via CSF1R signaling. Glia 69, 1583–1604. [PubMed: 33620118]

Meira M, Sievers C, Hoffmann F, Bodmer H, Derfuss T, Kuhle J, Haghikia A, Kappos L, and Lindberg RL (2019). PARP-1 deregulation in multiple sclerosis. Mult. Scler. J. Exp. Transl. Clin. 5, 2055217319894604. [PubMed: 31897308]

Mishra M, and Kowluru RA (2017). Role of PARP-1 as a novel transcriptional regulator of MMP-9 in diabetic retinopathy. Biochim. Biophys. Acta Mol. Basis Dis. 1863, 1761–1769. [PubMed: 28478229]

Moroni F (2008). Poly(ADP-ribose)polymerase 1 (PARP-1) and postischemic brain damage. Curr. Opin. Pharmacol. 8, 96–103. [PubMed: 18032109]

Moyon S, Huynh JL, Dutta D, Zhang F, Ma D, Yoo S, Lawrence R, Wegner M, John GR, Emery B, et al. (2016). Functional Characterization of DNA Methylation in the Oligodendrocyte Lineage. Cell Rep. 15, 748–760. [PubMed: 27149841]

Nguyen MV, Felice CA, Du F, Covey MV, Robinson JK, Mandel G, and Ballas N (2013). Oligodendrocyte lineage cells contribute unique features to Rett syndrome neuropathology. J. Neurosci. 33, 18764–18774. [PubMed: 24285883]

Nicolescu AC, Holt A, Kandasamy AD, Pacher P, and Schulz R (2009). Inhibition of matrix metalloproteinase-2 by PARP inhibitors. Biochem. Biophys. Res. Commun. 387, 646–650. [PubMed: 19619515]

Plane JM, Grossenbacher SK, and Deng W (2012). PARP-1 deletion promotes subventricular zone neural stem cells toward a glial fate. J. Neurosci. Res. 90, 1489–1506. [PubMed: 22431411]

Rowitch DH (2004). Glial specification in the vertebrate neural tube. Nat. Rev. Neurosci. 5, 409–419. [PubMed: 15100723]

Salmaso N, Jablonska B, Scafidi J, Vaccarino FM, and Gallo V (2014). Neurobiology of premature brain injury. Nat. Neurosci. 17, 341–346. [PubMed: 24569830]

Samudyata AE, Falcao A, Zubarev R, and Castelo-Branco G (2019). Long non-coding RNAs in the epegentic regulation of oligodendrocyte differentiation. Doctoral Thesis (Preprint). http://openarchive.ki.se/xmlui/handle/10616/46805.

Schüller U, Heine VM, Mao J, Kho AT, Dillon AK, Han YG, Huillard E, Sun T, Ligon AH, Qian Y, et al. (2008). Acquisition of granule neuron precursor identity is a critical determinant of progenitor cell competence to form Shh-induced medulloblastoma. Cancer Cell 14, 123–134. [PubMed: 18691547]

Scott GS, Virág L, Szabó C, and Hooper DC (2003). Peroxynitrite-induced oligodendrocyte toxicity is not dependent on poly(ADP-ribose) polymerase activation. Glia 41, 105–116. [PubMed: 12509801]

Scott GS, Kean RB, Mikheeva T, Fabis MJ, Mabley JG, Szabó C, and Hooper DC (2004). The therapeutic effects of PJ34 [N-(6-oxo-5,6-dihydrophenanthridin-2-yl)-N,N-dimethylacetamide.HCl], a selective inhibitor of poly(ADP-ribose) polymerase, in experimental allergic encephalomyelitis are associated with immunomodulation. J. Pharmacol. Exp. Ther. 310, 1053–1061. [PubMed: 15159442]

Selvaraj V, Soundarapandian MM, Chechneva O, Williams AJ, Sidorov MK, Soulika AM, Pleasure DE, and Deng W (2009). PARP-1 deficiency increases the severity of disease in a mouse model of multiple sclerosis. J. Biol. Chem. 284, 26070–26084. [PubMed: 19628872]

Semple BD, Blomgren K, Gimlin K, Ferriero DM, and Noble-Haeusslein LJ (2013). Brain development in rodents and humans: Identifying benchmarks of maturation and vulnerability to injury across species. Prog. Neurobiol. 106–107, 1–16.

Sharma K, Singh J, Pillai PP, and Frost EE (2015). Involvement of MeCP2 in Regulation of Myelin-Related Gene Expression in Cultured Rat Oligodendrocytes. J. Mol. Neurosci. 57, 176–184. [PubMed: 26140854]

Shi D, Xu S, Zhuo J, McKenna MC, and Gullapalli RP (2019). White Matter Alterations in Fmr1 Knockout Mice during Early Postnatal Brain Development. Dev. Neurosci. 41, 274–289. [PubMed: 32348987]

Stoica BA, Loane DJ, Zhao Z, Kabadi SV, Hanscom M, Byrnes KR, and Faden AI (2014). PARP-1 inhibition attenuates neuronal loss, microglia activation and neurological deficits after traumatic brain injury. J. Neurotrauma 31, 758–772. [PubMed: 24476502]

Szostak E, and Gebauer F (2013). Translational control by 3′-UTR-binding proteins. Brief. Funct. Genomics 12, 58–65. [PubMed: 23196851]

Tao X, Chen X, Hao S, Hou Z, Lu T, Sun M, and Liu B (2015). Protective actions of PJ34, a poly(ADP-ribose)polymerase inhibitor, on the blood-brain barrier after traumatic brain injury in mice. Neuroscience 291, 26–36. [PubMed: 25668593]

Thangaraj MP, Furber KL, Gan JK, Ji S, Sobchishin L, Doucette JR, and Nazarali AJ (2017). RNA-binding Protein Quaking Stabilizes Sirt2 mRNA during Oligodendroglial Differentiation. J. Biol. Chem. 292, 5166–5182. [PubMed: 28188285]

Veto S, Acs P, Bauer J, Lassmann H, Berente Z, Setalo G Jr., Borgulya G, Sumegi B, Komoly S, Gallyas F Jr., and Illes Z (2010). Inhibiting poly(ADP-ribose) polymerase: a potential therapy against oligodendrocyte death. Brain 133, 822–834. [PubMed: 20157013]

Wahlberg E, Karlberg T, Kouznetsova E, Markova N, Macchiarulo A, Thorsell AG, Pol E, Frostell Å, Ekblad T, Öncü D, et al. (2012). Family-wide chemical profiling and structural analysis of PARP and tankyrase inhibitors. Nat. Biotechnol. 30, 283–288. [PubMed: 22343925]

Wang ZQ, Auer B, Stingl L, Berghammer H, Haidacher D, Schweiger M, and Wagner EF (1995). Mice lacking ADPRT and poly(ADP-ribosyl)ation develop normally but are susceptible to skin disease. Genes Dev. 9, 509–520. [PubMed: 7698643]

Wang E, Aslanzadeh V, Papa F, Zhu H, de la Grange P, and Cambi F (2012). Global profiling of alternative splicing events and gene expression regulated by hnRNPH/F. PLoS ONE 7, e51266. [PubMed: 23284676]

Wang F, Yang YJ, Yang N, Chen XJ, Huang NX, Zhang J, Wu Y, Liu Z, Gao X, Li T, et al. (2018). Enhancing Oligodendrocyte Myelination Rescues Synaptic Loss and Improves Functional Recovery after Chronic Hypoxia. Neuron 99, 689–701.e5. [PubMed: 30078577]

Xu H, Dzhashiashvili Y, Shah A, Kunjamma RB, Weng YL, Elbaz B, Fei Q, Jones JS, Li YI, Zhuang X, et al. (2020). m⁶A mRNA Methylation Is Essential for Oligodendrocyte Maturation and CNS Myelination. Neuron 105, 293–309.e5. [PubMed: 31901304]

Zhang Y, Wang J, Ding M, and Yu Y (2013). Site-specific characterization of the Asp- and Glu-ADP-ribosylated proteome. Nat. Methods 10, 981–984. [PubMed: 23955771]

Zhang Y, Chen K, Sloan SA, Bennett ML, Scholze AR, O'Keeffe S, Phatnani HP, Guarnieri P, Caneda C, Ruderisch N, et al. (2014). An RNA-sequencing transcriptome and splicing database of glia, neurons, and vascular cells of the cerebral cortex. J. Neurosci. 34, 11929–11947. [PubMed: 25186741]

Zhang S, Rasai A, Wang Y, Xu J, Bannerman P, Erol D, Tsegaye D, Wang A, Soulika A, Zhan X, and Guo F (2018a). The Stem Cell Factor Sox2 Is a Positive Timer of Oligodendrocyte Development in the Postnatal Murine Spinal Cord. Mol. Neurobiol. 55, 9001–9015. [PubMed: 29623612]

Zhang S, Zhu X, Gui X, Croteau C, Song L, Xu J, Wang A, Bannerman P, and Guo F (2018b). Sox2 Is Essential for Oligodendroglial Proliferation and Differentiation during Postnatal Brain Myelination and CNS Remyelination. J. Neurosci. 38, 1802–1820. [PubMed: 29335358]

Zhang S, Kim B, Zhu X, Gui X, Wang Y, Lan Z, Prabhu P, Fond K, Wang A, and Guo F (2020). Glial type specific regulation of CNS angiogenesis by HIFα-activated different signaling pathways. Nat. Commun. 11, 2027. [PubMed: 32332719]

Zhang S, Wang Y, Xu J, Kim B, Deng W, and Guo F (2021a). HIFα Regulates Developmental Myelination Independent of Autocrine Wnt Signaling. J. Neurosci. 41, 251–268. [PubMed: 33208471]

Zhang S, Wang Y, Zhu X, Song L, Zhan X, Ma E, McDonough J, Fu H, Cambi F, Grinspan J, and Guo F (2021b). The Wnt Effector TCF7l2 Promotes Oligodendroglial Differentiation by Repressing Autocrine BMP4-Mediated Signaling. J. Neurosci. 41, 1650–1664. [PubMed: 33452226]

Zhao C, Deng Y, Liu L, Yu K, Zhang L, Wang H, He X, Wang J, Lu C, Wu LN, et al. (2016). Dual regulatory switch through interactions of Tcf7l2/Tcf4 with stage-specific partners propels oligodendroglial maturation. Nat. Commun. 7, 10883. [PubMed: 26955760]

Zhen Y, and Yu Y (2018). Proteomic Analysis of the Downstream Signaling Network of PARP1. Biochemistry 57, 429–440. [PubMed: 29327913]

Zhou X, He C, Ren J, Dai C, Stevens SR, Wang Q, Zamler D, Shingu T, Yuan L, Chandregowda CR, et al. (2020). Mature myelin maintenance requires Qki to coactivate PPARβ-RXRα-mediated lipid metabolism. J. Clin. Invest. 130, 2220–2236. [PubMed: 32202512]

Highlights

- PARP1 drives oligodendroglial development and regeneration

- The PARylation activity mediates PARP1-regulated OPC differentiation

- Proteomics identifies PARP1 target proteins involved in RNA metabolism

- PARP1-modulated Myef2 controls myelin gene expression and OPC differentiation
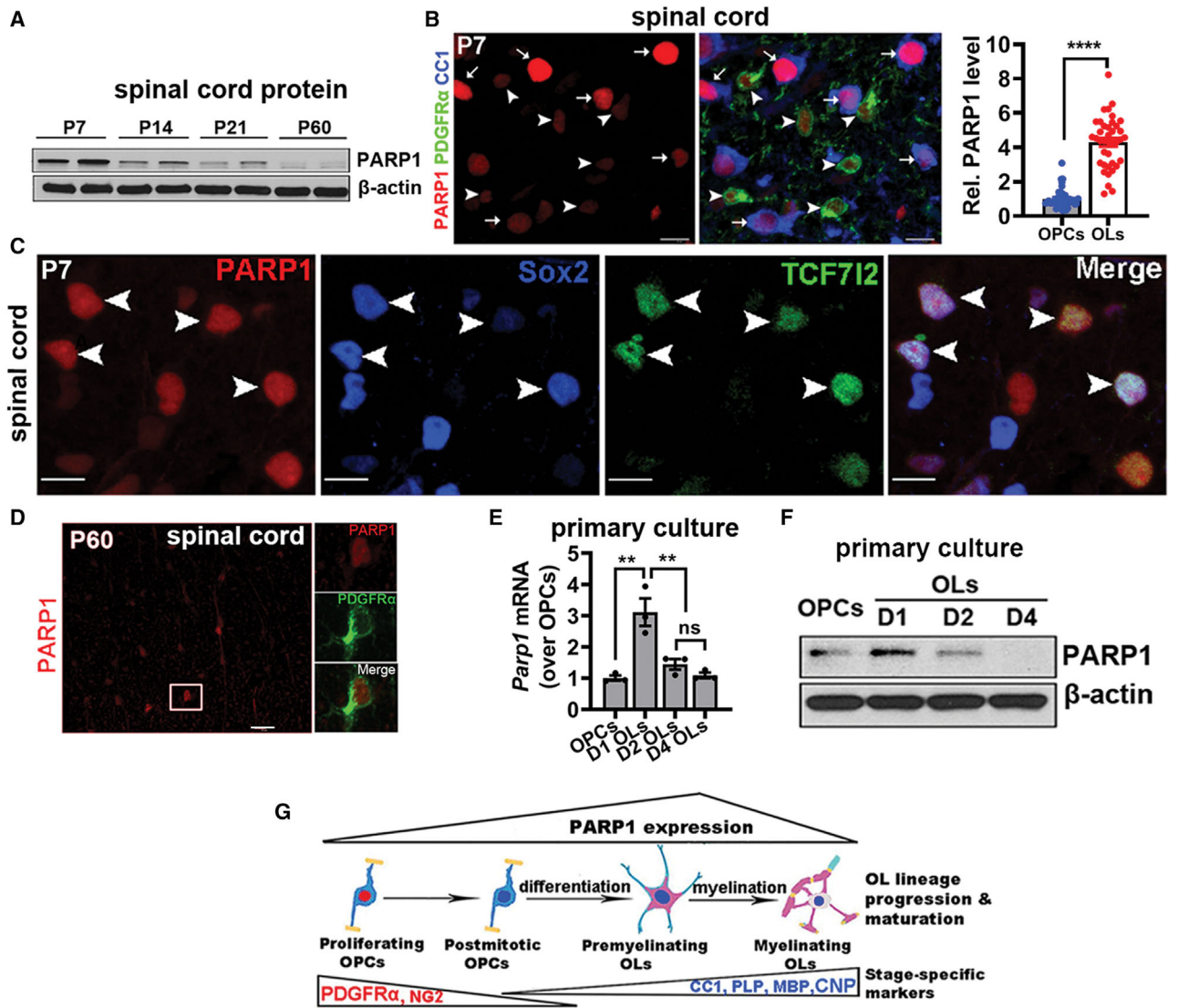
Figure 1. PARP1 expression along oligodendrocyte lineage progression and maturation

(A) Western blotting (WB) of PARP1 (postnatal day [P]). β-actin, loading control.

(B) Triple immunohistochemistry (IHC) assay of PARP1, PDGFRα, and CC1. Arrowheads, OPCs; arrows, OLs. *P* value, please see Table S4.

(C) IHC of PARP1, Sox2, and TCF7l2, a marker of newly differentiated OLs.

(D) IHC of PARP1 in adult spinal cord.

(E and F) qRT-PCR and WB of PARP1 in primary OPCs and differentiated OLs at D1 to D4.

</p/> (G) Diagram summarizing the temporal dynamics of PARP1 during OL development.

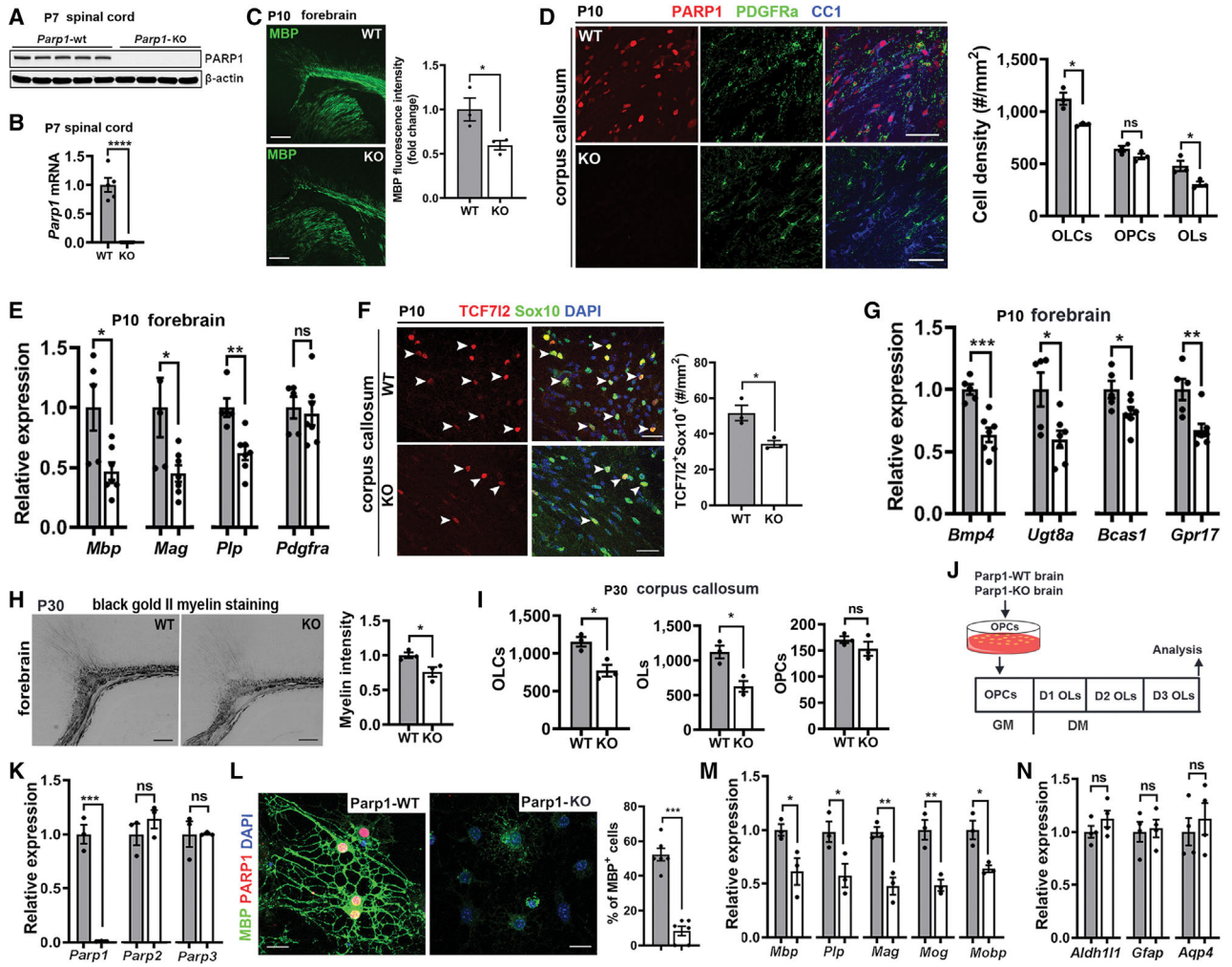Scale bars: (B and C) 10 μm; (D) 20 μm.

Figure 2. PARP1 deficiency impairs OL maturation and results in hypomyelination during postnatal development

(A) WB of PARP1 protein in *Parp1* WT and KO mice.

(B) qRT-PCR assay for *Parp1* mRNA.

(C) IHC and quantification of myelin by myelin basic protein (MBP).

(D) Representative images and density of Sox10$^+$ OLCs, Sox10$^+$PDGFRα$^+$ OPCs, and Sox10$^+$CC1$^+$ OLs.

(E) qRT-PCR assay for myelin genes and *Pdgfra*.

(F) IHC and quantification of TCF7l2$^+$Sox10$^+$ newly differentiated OLs.

(G) qRT-PCR assay for genes encoding markers of pre-myelination OLs.

(H) Black-Gold II myelin staining and quantification in P30 brain.

(I) Density (#/mm^2) of Sox10$^+$ OLCs, Sox10$^+$CC1$^+$ OLs, and Sox10$^+$PDGFRα$^+$ OPCs.

(J) Experimental design of purified primary cultures for (K)–(N). GM, growth medium; DM, differentiation medium.

(K) qRT-PCR assay for *Parp1–3* mRNA.

(L) IHC and quantification of MBP$^+$ ramified cells among DAPI$^+$ cells.

(M and N) qRT-PCR assay for myelin-specific genes (M) and astrocyte-specific genes (N).

Scale bars: (C and H) 200 μm; (D and F) 50 μm; (L) 10 μm. Gray bars: WT; white bars: *Parp1* KO.
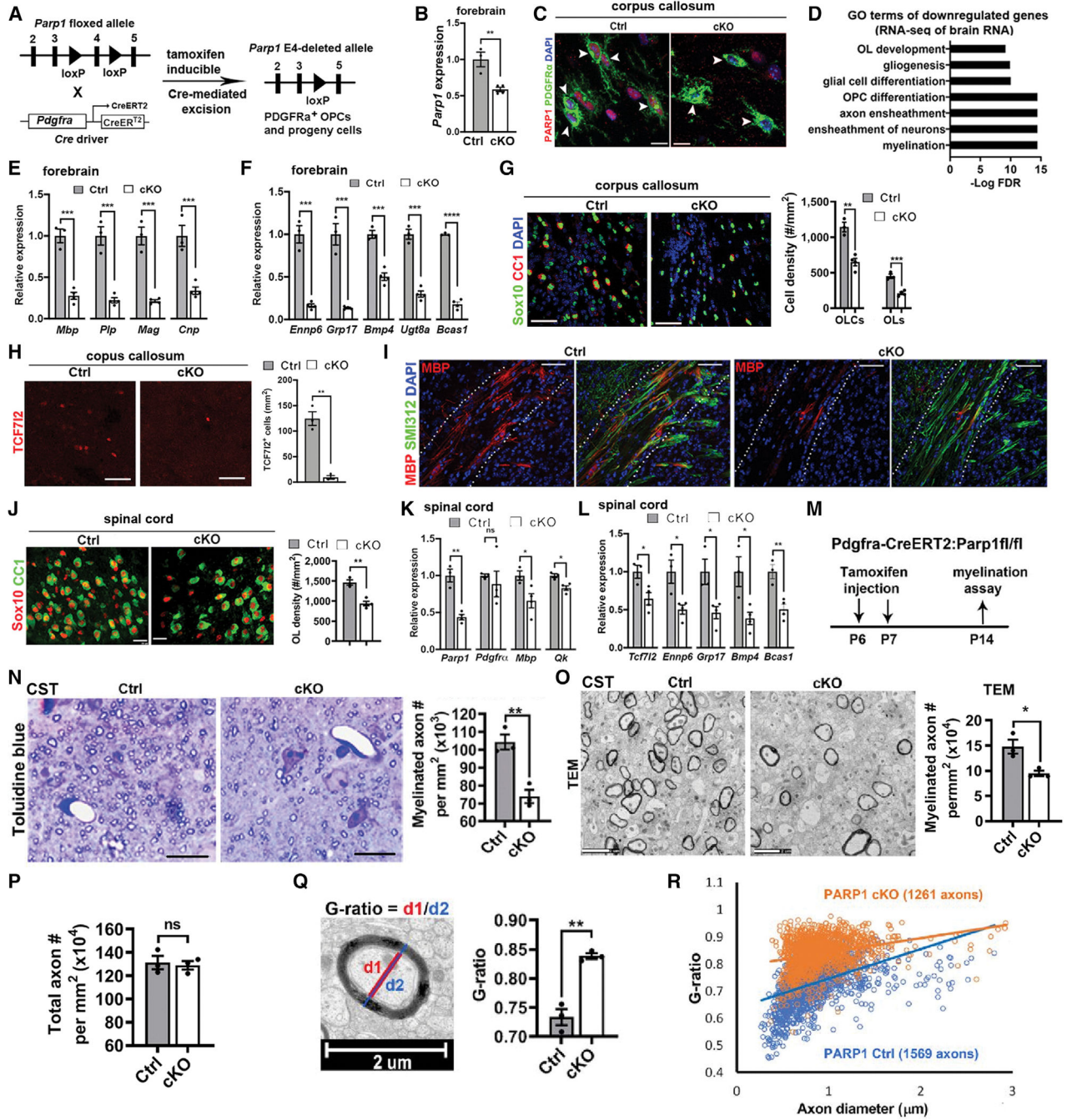
Figure 3. OPC-specific PARP1 cKO inhibits OPC differentiation and myelination

(A) Diagram depicting inducible Pdgfrα:Parp1 cKO. Tamoxifen injection at P1, P2, and P3, and data analysis (B–L) at P9.

(B) qRT-PCR assay of *Parp1* mRNA in the forebrain.

(C) Confocal images showing PARP1 depletion in PDGFRα+ OPCs (arrowheads).

(D) Gene Ontology (GO) of top enriched biological processes for downregulated genes (cKO versus Ctrl) in the brain (Table S2).

(E and F) qRT-PCR assays for genes coding myelin-specific proteins (E) and pre-myelinating OL markers (F).

(G and H) IHC assay for $Sox10^+$ OLCs, $Sox10^+CC1^+$ OLs, and TCF7l2-expressing newly differentiated OLs.

(I) IHC of MBP and axonal marker SMI312 in the external capsule (dotted areas).

(J) IHC assay for $Sox10^+CC1^+$ OLs in the ventral white matter.

(K and L) qRT-PCR assays for mRNA of indicated genes in the spinal cord.

(M) Experimental design for (N)–(R). Corticospinal tract (CST) was used for analysis.

(N) Myelination assay by toluidine blue myelin staining on semithin (500 nm) sections.

(O and P) Myelination assay by transmission electron microscopy (TEM) on ultrathin (50 nm) sections. Axons with diameter 0.3 μm were included for analysis.

(Q) Diagram and analysis of average G-ratio of myelinated axons.

(R) Plot of individual G-ratio versus axons.

Scale bars: (O) 2 μm; (C, J, and N) 10 μm; (G–I), 50 μm.
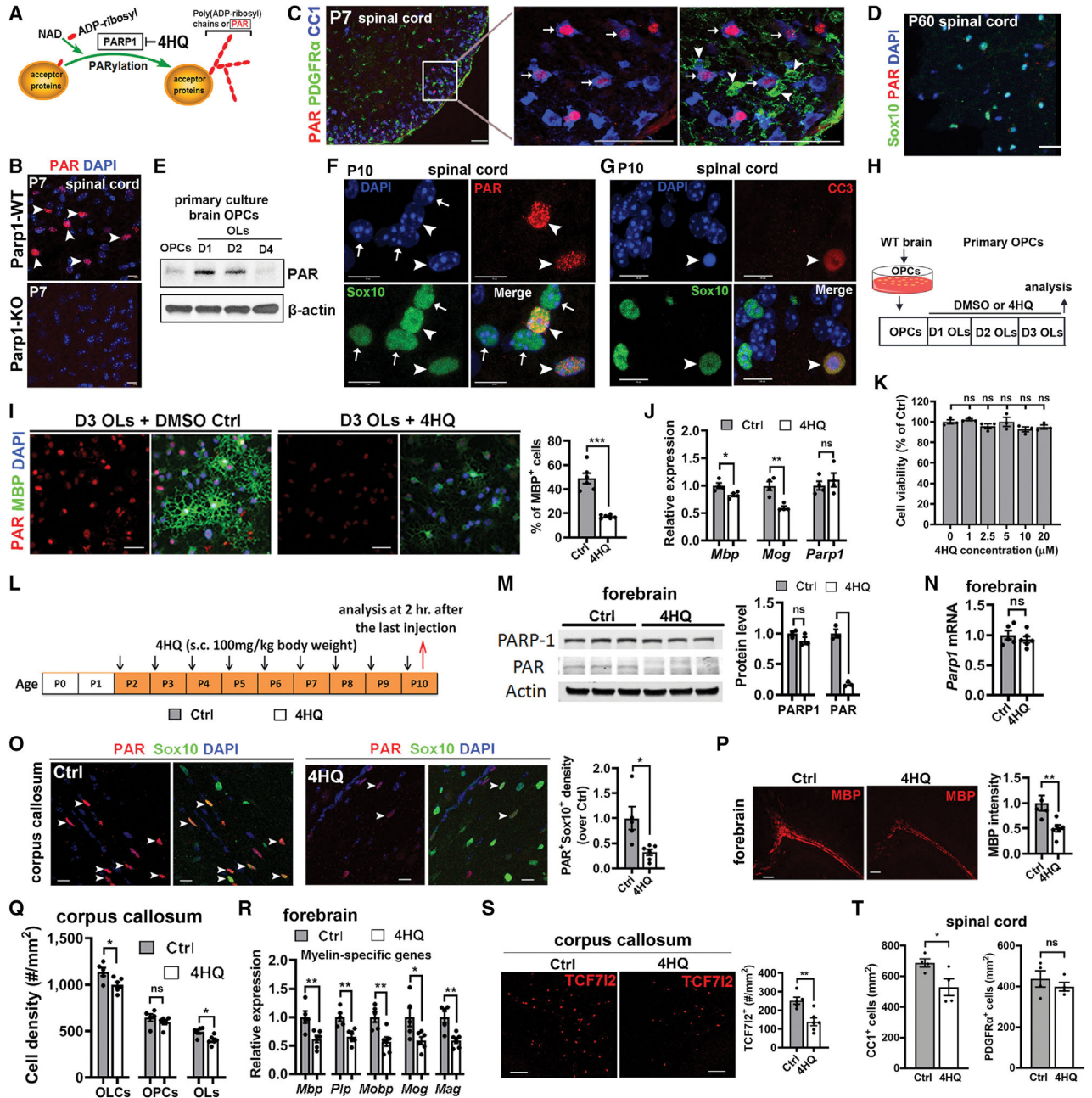
Figure 4. PARP1 activity is essential for OPC differentiation

(A) Diagram depicting 4-hydoxyquinazoline (4HQ) inhibition of PARP1-mediated PARylation.

(B) IHC of PAR in P7 spinal cord. PAR signals were abolished in *Parp1* KO mice.

(C) Triple IHC of PAR, PDGFRα, and CC1 in P7 spinal cord. Arrowheads, PDGFRα+ OPCs; arrows, CC1+ OLs.

(D) Absence of PAR signals from Sox10+ cells in P60 spinal cord.

(E) WB of PAR using primary brain OPCs and differentiating OLs at D1, D2, and D4.

(F) High-power images showing indistinguishable morphology between PAR+Sox10+ (arrowheads) and PAR−Sox10+ (arrows) nuclei (DAPI+) in spinal white matter.

(G) IHC showing the condensation of DAPI$^+$ nucleus of an apoptotic OL (active cleaved caspase 3 (CC3)$^+$Sox10$^+$, arrowheads) in spinal white matter.

(H) Experimental design for (I)–(K). 4HQ was used at 10 μM.

(I) Immunocytochemistry (ICC) of MBP and PAR.

(J) qRT-PCR assay for indicated genes.

(K) MTT cell survival assay of D3 OLs treated with different doses of 4HQ.

(L) Experimental design for (M)–(T).

(M) WB assay for PARP1 and PAR.

(N) qRT-PCR assay for brain *Parp1* mRNA.

(O) IHC assay for PAR and Sox10 in the corpus callosum (CC).

(P) Myelination assay by MBP IHC.

(Q) Densities of Sox10$^+$ OLCs, Sox10$^+$PDGFRα$^+$ OPCs, and Sox10$^+$CC1$^+$ OLs.

(R) qRT-PCR assays for indicated myelin-specific genes.

(S) IHC assay for TCF7l2$^+$ newly differentiated OLs.

(T) Density of CC1$^+$ OLs and PDGFRα$^+$ OPCs in the spinal cord white matter.

Scale bars: (B, F, and G) 10 μm; (I and O) 20 μm; (C, D, and S) 50 mm; (O) 200 μm.
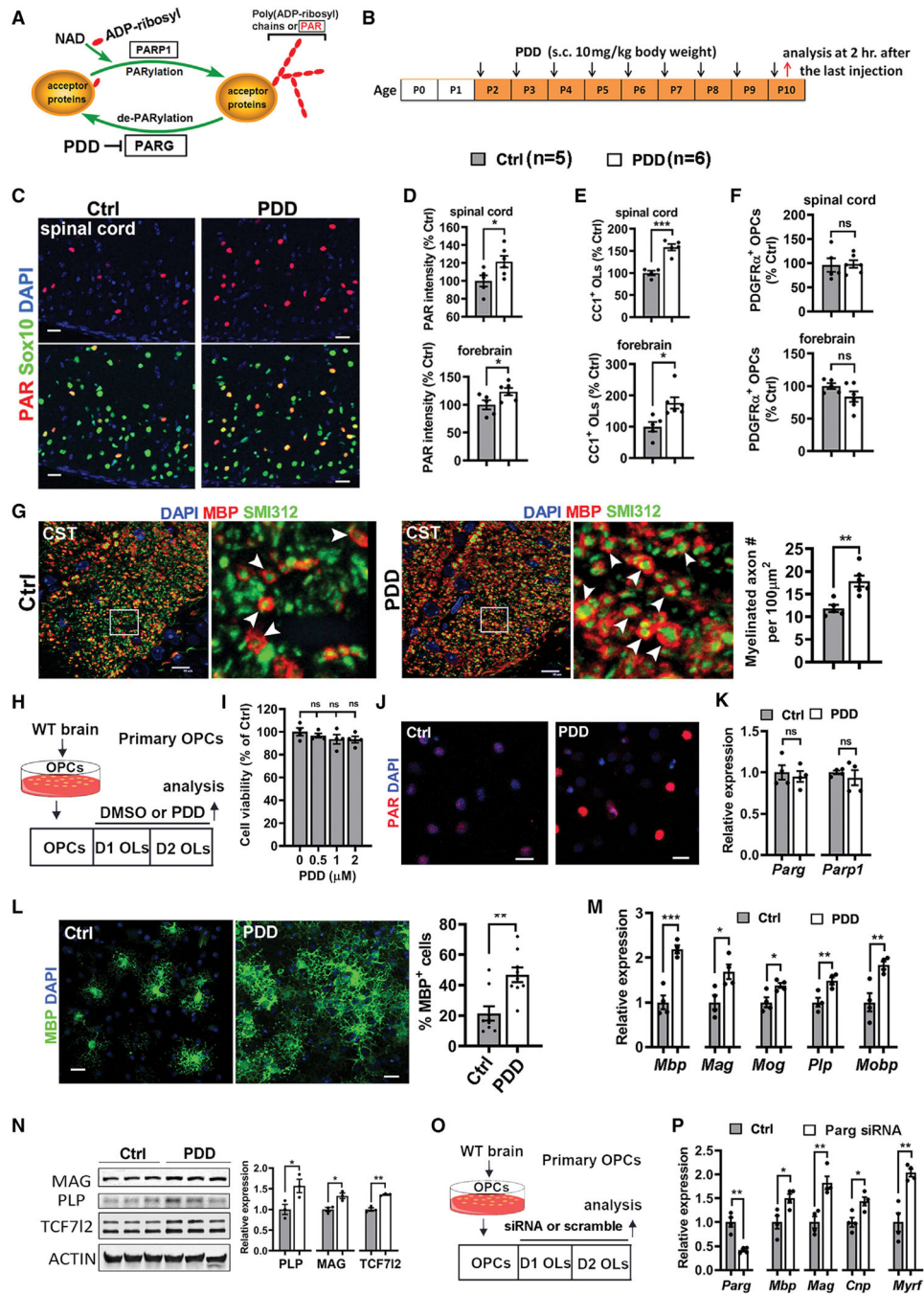
Figure 5. Stabilizing PARylation promotes OPC differentiation

(A) Diagram depicting PARylation stabilization by inhibiting PARG.

(B) Experimental design for (C)–(G).

(C) Confocal images of PAR and Sox10 in the ventral white matter.

(D–F) Percentage of PAR intensity (D), CC1+ OLs (E), and PDGFRα+ OPCs (F) in spinal white matter and forebrain CC.

(G) Myelination assay in the CST by myelin marker MBP and axon marker SMI312.

(H) Experimental design for (I)–(N). PDD was used at 1 μM.

(I) MTT cell survival assay of D2 OLs at different PDD doses.

(J) Confocal images showing increased intensity PAR in PDD-treated cultures.

(K) qRT-PCR assay for *Parg and Parp1.*

(L) ICC assay for MBP[+] OLs among DAPI^{+} cells.

(M) qRT-PCR assay for indicated myelin-associated genes.

(N) WB and quantification of myelin proteins MAG, PLP, and pre-myelinating OL marker TCF7l2.

(O and P) qRT-PCR assay for indicated genes in the presence of *Parg* siRNA or scramble control for 2 days prior to analysis.

Scale bars: (C) 25 μm; (G, J, and L) 10 μm.
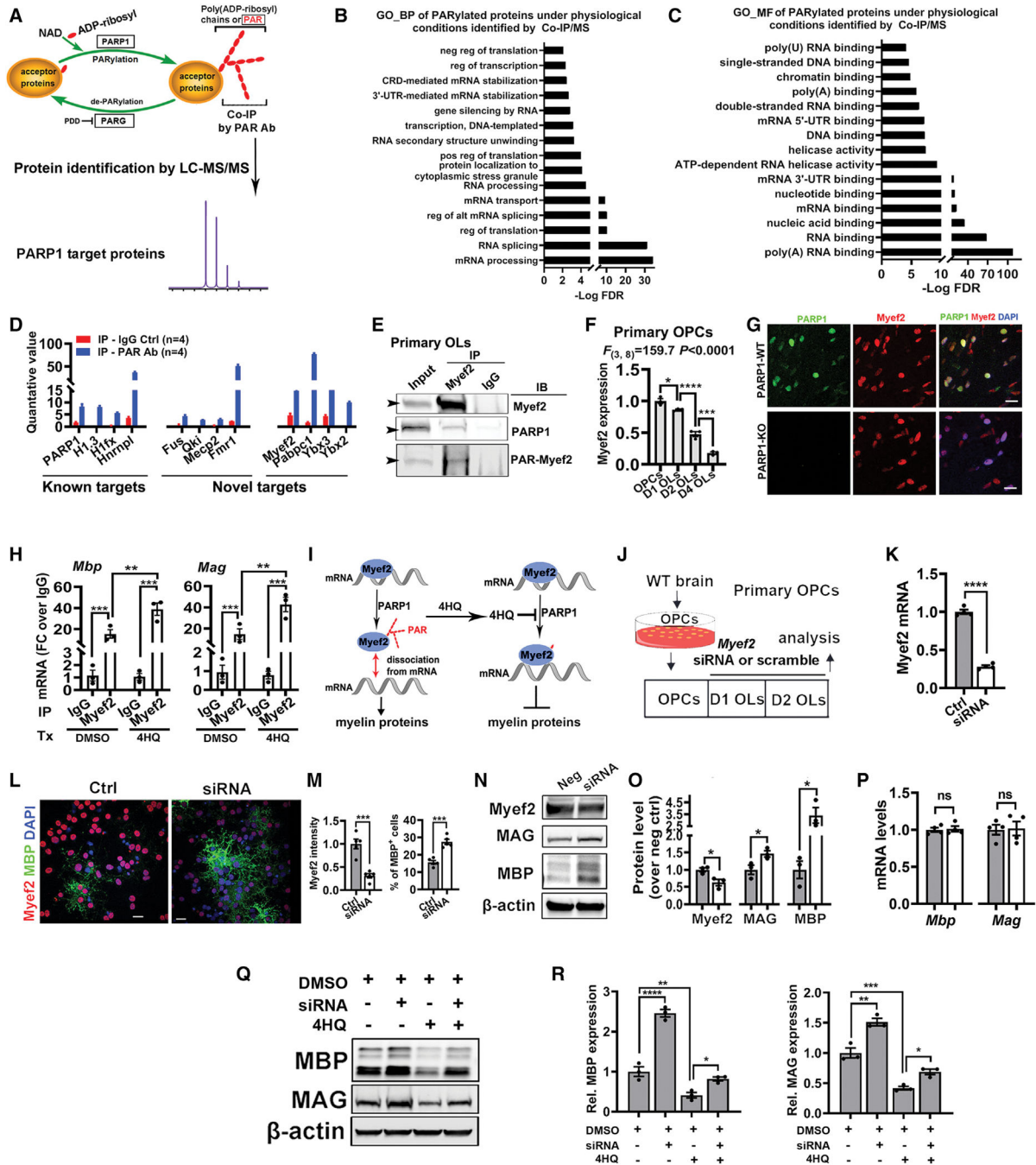
Figure 6. PARP1 PARylates Myef2 to regulate OPC differentiation and myelin gene expression

(A) Flow chart showing identification of PARylated acceptor proteins. Whole protein was prepared from the spinal cord of P7 mice 30 min after PDD injection to stabilize PARylation.

(B and C) GO analysis of biological processes (B) and molecular function (C) of the 131 potential PARylated acceptor proteins (Table S3).

(D) Selected examples of known PARylated proteins and potential PARylated proteins.

(E) Co-IP/WB assay confirming the interaction between Myef2 and PARP1 and the presence of PARylated Myef2 at the molecular weight of Myef2 (~55 kD) in D2 primary OLs.

(F) qRT-PCR assay for Myef2 in primary OPCs and differentiating OLs.

(G) Double IHC of PARP1 and Myef2 in the CC of P7 *Parp1*-WT and KO mice.

(H) Abundance of *Mbp* and *Mag* mRNA in the immunoprecipitates by RNA immunoprecipitation (RIP) using Myef2 antibody or IgG Ctrl in D2 primary OLs treated with DMSO or 4HQ treated.

(I) Schematic conclusion of (H), PARP1 inhibition by 4HQ potentiates the binding of Myef2 to mRNA molecules.

(J) Experimental design for (K)–(P).

(K) qRT-PCR assay for *Myef2* mRNA.

(L and M) ICC assay for Myef2 and MBP in Ctrl and *Myef2* siRNA-treated primary OLs.

(N and O) WB assay of Myef2 and myelin proteins MAG and MBP.

(P) qRT-PCR assay for *Mbp* and *Mag.*

(Q and R) WB assay for MBP and MAG in D2 primary OLs treated with DMSO Ctrl, *Myef2* siRNA, 4HQ, and *Myef2* siRNA[+]4HQ for 48 hours in the differentiation medium.

Scale bars: (G) 20 μm; (L) 10 μm.
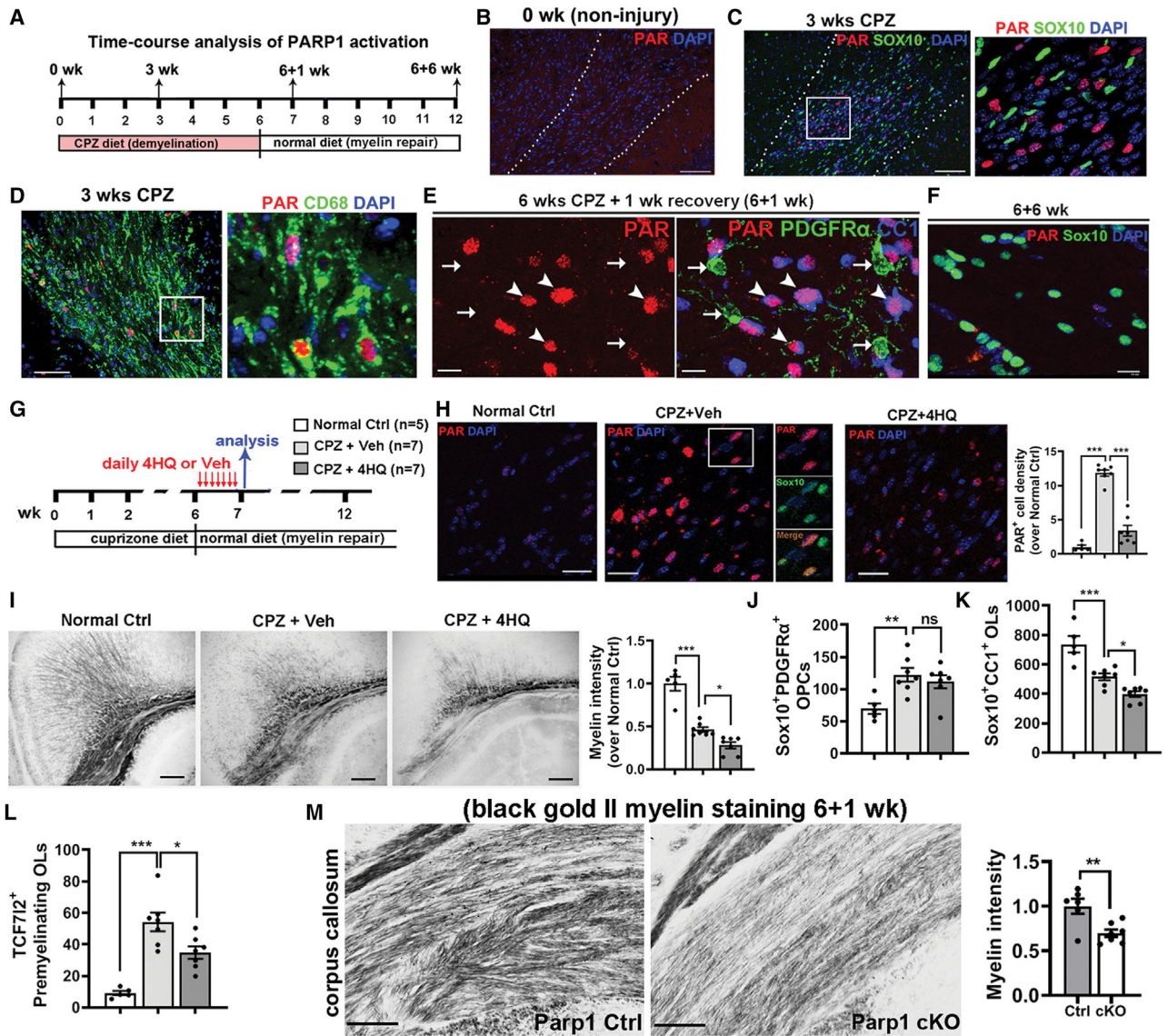
Figure 7. PARP1 activity is required for oligodendrocyte regeneration and remyelination

(A) Experimental design of time-course analysis (B–F) in the CC of cuprizone (CPZ)-induced demyelination and remyelination.

(B) IHC showing absence of PAR in healthy mice.

(C and D) Double IHC of PAR and oligodendroglial marker Sox10 (C) and activated microglial marker CD68 (D) after 3 weeks of CPZ. Boxed areas are shown on the right.

(E) IHC of PAR/CC1/PDGFRα in the CC at 6+1 weeks.

(F) IHC showing absence of PAR$^+$/Sox10$^+$ cells at 6+6 weeks.

(G) Experimental design for (H)–(L). Daily injection of 4HQ (100 mg/kg) on day 1 after returning to the normal diet for 7 days, and the posterior CC was processedfor analysis.

(H) IHC assay for PAR$^+$Sox10$^+$ cells. Boxed area is shown for individual Sox10 and PAR channels.

(I) Myelination assay by Black-Gold II myelin staining.

(J–L) Density (#/mm^2) of Sox10$^+$PDGFRα$^+$ OPCs, Sox10$^+$CC1$^+$ OLs, and TCF7l2$^+$ premyelinating OLs in the CC.

(M) Black-Gold II myelin assay in the middle CC of *Parp1* cKO and Ctrl mice at 6+1 weeks (Figure S7B).

Scale bars: (B–D) 100 mm; (E and F) 10 μm; (H) 20 μm; (I and N) 50 μm.

KEY RESOURCES TABLE

REAGENT or RESOURCE	SOURCE	IDENTIFIER
Antibodies		
Rabbit PARP1 N-terminal antibody (pAb)	Active Motif	Cat#39559; RRID: AB_2793257
Mouse PARP1 monoclonal antibody	Proteintech	Cat#66520-1-Ig; RRID: AB_2881883
Anti-poly-ADP-ribose binding reagent	Millipore	Cat#MABE1031; RRID: AB_2665467
Mouse monoclonal Anti-PAR antibody	Trevigen	Cat#4335-MC-100; RRID: AB_2572318
Goat polyclonal Sox2 (Y-17)	Santa Cruz Biotechnology	Cat#sc-17320; RRID: AB_2286684
Mouse monoclonal APC (Ab-7) (CC1)	Millipore	Cat#OP80; RRID: AB_213434
Rabbit monoclonal TCF4/TCF7L2 (C48H11)	Cell Signaling Technology	Cat#2569S; RRID: AB_2199816
Mouse Monoclonal TCF7L2 (6h5-3)	Millipore	Cat#05-511; RRID: AB_309772
Goat polyclonal PDGFRα	R&D System	Cat# AF1062; RRID: AB_2236897
Chicken Polyclonal EYFP	Millipore	Cat#06-896; RRID: AB_310288
Rabbit polyclonal Sox10	Abcam	Cat# ab27655; RRID: AB_778021
Rat monoclonal MBP	Novus	Cat# NB600-717; RRID: AB_2139899
Rabbit polyclonal Myef2	Proteintech	Cat#16051-1-AP; RRID: AB_2146869
Mouse monoclonal SMI312	BioLegend	Cat#837801; RRID: AB_2565383
Goat polyclonal AIF-1/Iba1	Novus	Cat# NB100-1028; RRID: AB_521594
Mouse monoclonal GFAP	Millipore	Cat# MAB360; RRID: AB_2275425
Rabbit polyclonal NG2	Millipore	Cat#AB5320; RRID: AB_91789
Purified anti-mouse CD90.2 Antibody	Biolegend	Cat#105302; RRID: AB_313173
Rabbit polyclonal Myef2	Proteintech	Cat#16051-1-AP; RRID: AB_2146869
Rabbit polyclonal MAG	Millipore	Cat#AB1567; RRID: AB_2110397
Rabbit polyclonal PLP	Thermo Fisher Scientific	Cat# PA3-151; RRID: AB_2165785
Rabbit polyclonal TLE3	Proteintech	Cat#11372-1-AP; RRID: AB_2203743
Rabbit polyclonal AIF	Abcam	Cat# ab1998; RRID: AB_302748
Rabbit polyclonal Gasdermin D (L60)	Cell Signaling Technology	Cat#93709; RRID: AB_2800210
Mouse monoclonal MLKL	Proteintech	Cat#66675-1-Ig; RRID: AB_2882029
Rabbit monoclonal Phospho-MLKL (S345) (D6E3G)	Cell Signaling Technology	Cat#D6E3G; RRID: AB_2799112
Rabbit polyclonal β-actin	Cell Signaling Technology	Cat#4967L; RRID: AB_330288
HRP goat anti-rabbit IgG (H+L)	Thermo Fisher Scientific	Cat#31460; RRID: AB_228341

REAGENT or RESOURCE	SOURCE	IDENTIFIER
HRP goat anti-mouse IgG (H+L)	Thermo Fisher Scientific	Cat#31430; RRID: AB_228307
HRP goat anti-rat IgG	Cell Signaling Technology	Cat#7077; RRID: AB_10694715
HRP donkey anti-goat IgG (H+L)	Thermo Fisher Scientific	Cat#A15999; RRID: AB_2534673
Normal rabbit IgG control antibody	Cell Signaling Technology	Cat#2729; RRID: AB_1031062
Normal goat IgG control antibody	R&D Systems	Cat#AB-108-C; RRID: AB_354267
Alexa Fluor® 488 AffiniPure F(ab')₂ Fragment Donkey Anti-Goat IgG (H+L)	Jackson Immuno Research Laboratories	Cat#705-546-147; RRID: AB_2340430
Alexa Fluor® 594 AffiniPure F(ab')₂ Fragment Donkey Anti-Goat IgG (H+L)	Jackson Immuno Research Laboratories	Cat#705-586-147; RRID: AB_2340434
Alexa Fluor® 488 AffiniPure F(ab')₂ Fragment Donkey Anti-Rabbit IgG (H+L)	Jackson Immuno Research Laboratories	Cat#711-546-152; RRID: AB_2340619
Alexa Fluor® 594 AffiniPure F(ab')₂ Fragment Donkey Anti-Rabbit IgG (H+L)	Jackson Immuno Research Laboratories	Cat#711-586-152; RRID: AB_2340622
Alexa Fluor® 594 AffiniPure F(ab')₂ Fragment Donkey Anti-Rat IgG (H+L)	Jackson Immuno Research Laboratories	Cat#712-586-153; RRID: AB_2340691
Alexa Fluor® 488 AffiniPure F(ab')₂ Fragment Donkey Anti-Mouse IgG (H+L)	Jackson Immuno Research Laboratories	Cat#715-546-150; RRID: AB_2340849
Alexa Fluor® 594 AffiniPure F(ab')₂ Fragment Donkey Anti-Mouse IgG (H+L)	Jackson Immuno Research Laboratories	Cat#715-586-150; RRID: AB_2340857
Biotin-SP (long spacer) AffiniPure F(ab')₂ Fragment Donkey Anti-Mouse IgG (H+L)	Jackson Immuno Research Laboratories	Cat#715-066-151; RRID: AB_2340788
Chemicals, peptides, and recombinant proteins		
4-hydroxyquinazoline	Sigma-Aldrich	Cat#H57807
PDD 00017273	MedChemExpress	Cat#HY-108360
DMSO	Sigma-Aldrich	Cat#T5648
Tamoxifen	Sigma-Aldrich	Cat#T5648
Ethanol	KOPTEC	Cat#DSP-MD-43
Methanol	BDH	Cat#BDH1135-4LP
Sunflower seed oil	Sigma-Aldrich	Cat#47123
Paraformaldehyde	Electron Microscopy Science	Cat#1570-S
Sucrose	Fisher Scientific	Cat#S5-500
O.C.T. compound	VWR International	Cat#361603E
Normal donkey serum	Jackson Immuno Research Laboratories	Cat#017-000-121
DAPI	Sigma-Aldrich	Cat#D9542
Xylene	Sigma-Aldrich	Cat#534056
Mounting medium	Fisher Scientific	Cat#SP15-100
Glutaraldehyde	Electron Microscopy Science	Cat#16130

REAGENT or RESOURCE	SOURCE	IDENTIFIER
0.2 M sodium cacodylate buffer	Electron Microscopy Science	Cat#11653
2% (w/v) aqueous osmium tetroxide	Electron Microscopy Science	Cat#19152
Propylene oxide	Electron Microscopy Science	Cat#20401
Toluidine blue	Ted Pella Inc	Cat#19451
Papain	Worthington	Cat#LK003176
DNase I	Sigma	Cat#D5025
D-(+)-glucose	Amresco	Cat#0188
DMEM medium	Thermo Fisher Scientific	Cat#1196092
Fetal bovine serum	Sigma-Aldrich	Cat#12306-C
Penicillin/streptomycin	Thermo Fisher Scientific	Cat#15140122
Poly-D-lysine	Millipore	Cat#A003-E
HBSS	Thermo Fisher Scientific	Cat#24020117
Insulin	Sigma-Aldrich	Cat#I6634
Apo-transferrin	Sigma-Aldrich	Cat#T2036
Putrescine	Sigma-Aldrich	Cat#P5780
Sodium selenite	Sigma-Aldrich	Cat#S5261
Progesterone	Sigma-Aldrich	Cat#P0130
FGF	Peprotech	Cat#450-33
PDGF-AA	Peprotech	Cat#315-17
Forskolin	Peprotech	Cat#6652995
Glutamax	Thermo Fisher Scientific	Cat#35050
F12/high-glucose DMEM	Thermo Fisher Scientific	Cat#11330032
Transferrin	Sigma-Aldrich	Cat#T8158
3,3′,5-Triiodo-L-thyronine	Sigma-Aldrich	Cat#T5516
L-Thyroxine	Sigma-Aldrich	Cat#T0397
MTT	Sigma-Aldrich	Cat#M5655
N-PER Neuronal Protein Extraction Reagent	Thermo Fisher Scientific	Cat#87792
Halt protease and phosphatase inhibitor cocktail	Thermo Fisher Scientific	Cat#78446
PMSF	Cell Signaling Technology	Cat#8553S
BSA	Cell Signaling Technology	Cat#9998
Pierce IP Lysis/Wash Buffer	Thermo Fisher Scientific	Cat#87787

REAGENT or RESOURCE	SOURCE	IDENTIFIER
β-mercaptoethanol	BIO-RAD	Cat#1610710
Trypsin gold	Promega	Cat#V528A
RNaseOUT	Thermo Fisher Scientific	Cat#10777019
Protease inhibitor	Cell Signaling Technology	Cat#5871
Protein G Dynabeads	Life Technologies	Cat#10003D
HiPerFect transfection reagent	QIAGEN	Cat#301705
Streptavidin, Pacific Blue conjugate	Thermo Fisher Scientific	Cat#S11222
10x PBS	K-D Medical	Cat#RGF-3210
20x TBS	K-D Medical	Cat#RGF-3346
10X TAE	K-D Medical	Cat#RGF-3310
10X Tris/Glycine/SDS buffer	BIO-RAD	Cat#1610772
Tween-20	Sigma-Aldrich	Cat# T8787
Triton X-100	Sigma-Aldrich	Cat# P9416
Critical commercial assays		
Black-Gold II myelin stain	Millipore	Cat#AG105
BCA protein assay kit	Thermo Fisher Scientific	Cat#23225
Pierce Crosslink Magnetic IP/Co-IP kit	Thermo Fisher	Cat#88805
protein A/G magnetic beads	Thermo Fisher	Cat#88802
Pierce Classic Magnetic IP/Co-IP kit	Thermo Fisher	Cat#88804
RNeasy Lipid Tissue Mini Kit	QIAGEN	Cat#74804
RNase-Free DNase Set	QIAGEN	Cat#79254
QIAGEN Omniscript RT Kit	QIAGEN	Cat#205111
QuantiTect SYBR® Green PCR Kit	QIAGEN	Cat#204145
NEBNext Ultra Directional RNA Library Prep Kit	New England BioLabs	Cat#E7420
Pierce Quantitative Fluorometric Peptide Assay	Thermo Fisher Scientific	Cat#23290
Trans-blot turbo RTA midi 0.2 μm nitrocellulose transfer kit	BIO-RAD	Cat#1704271
Western Lightening Plus ECL	Perkin Elmer	Cat#NEL103001EA
EMbed 812 Kit for Electron Microscopy Embedding	Electron Microscopy Science	Cat#14120
Deposited data		

REAGENT or RESOURCE	SOURCE	IDENTIFIER
Bulk brain RNA-seq	GEO	GEO: GSE181933
Western blot images, uncropped	Mendeley	https://doi.org/10.17632/726pr7csxz.1
Experimental models: Cell lines		
B104-1-1 neuroblastoma	ATCC	Cat# CRL-1887
Experimental models: Organisms/strains		
Parp1 knockout mice	Jackson Laboratory	RRID: IMSR_JAX:002779
Parp1-floxed mice	provided by Dr. Kraus (Luo et al., 2017)	RRID: IMSR_JAX:032650
Olig2-Cre	Jackson Laboratory	RRID: IMSR_JAX:025567
Pdgfra-CreER^{T2}	Jackson Laboratory	RRID: IMSR_JAX:018280
Rosa26-LoxP-STOP-LoxP-EYFP	Jackson Laboratory	RRID: IMSR_JAX:006148
C57BL6J	Jackson Laboratory	RRID: IMSR_JAX:000664
Oligonucleotides		
see Table S5	N/A	N/A
Software and algorithms		
ImageJ	ImageJ public	https://imagej.net/software/fiji/downloads
X! Tandem Alanine (2017.2.1.4)	The GPM, thegpm.org	https://www.thegpm.org/tandem/
Scaffold_4.8.4	Proteome Software Inc.	https://www.proteomesoftware.com
TopHat version 2.0.12	Center for computational biology	https://ccb.jhu.edu/software/tophat/downloads/
DESeq version 2.1.6.3	Bioconductor	https://bioconductor.org/packages/release/bioc/html/DESeq2.html
HTseq v0.6.1	HTseq	https://htseq.readthedocs.io/en/master/
STAR version2.5	Spliced Transcripts Alignment to a Reference	https://code.google.com/archive/p/ma-star/
National Institutes of Health online tool DAVID	National Institutes of Health	https://david.nciferf.gov/
Other		

REAGENT or RESOURCE	SOURCE	IDENTIFIER
AnykD Mini-PROTEAN TGX precast gels	BIO-RAD	456-9035
7.5% Mini-PROTEAN TGX precast gels	BIO-RAD	456-8024
0.2% cuprizone diet	Envigo	TD.140800